



The track-length extension fitting algorithm for energy measurement of interacting particles in liquid argon TPCs and its performance with ProtoDUNE-SP data







The DUNE Collaboration




A. Abed Abud,³⁵ B. Abi,¹⁵⁷ R. Acciarri,⁶⁶ M. A. Acero,¹² M. R. Adames,¹⁹⁴ G. Adamov,⁷²
 M. Adamowski,⁶⁶ D. Adams,²⁰ M. Adinolfi,¹⁹ C. Adriano,³⁰ A. Aduszkiewicz,⁸¹
 J. Aguilar,¹²⁷ F. Akbar,¹⁷⁶ N. S. Alex,¹⁷⁶ K. Allison,⁴³ S. Alonso Monsalve,³⁵
 M. Alrashed,¹²⁰ A. Alton,¹³ R. Alvarez,³⁹ T. Alves,⁸⁸ H. Amar,⁸⁴ P. Amedo,^{85,84}
 J. Anderson,⁸ C. Andreopoulos,¹²⁹ M. Andreotti,^{94,67} M. P. Andrews,⁶⁶ F. Andrianala,⁵
 S. Andringa,¹²⁸ N. Anfimov , A. Ankowski,¹⁸⁵ D. Antic,¹⁹ M. Antoniassi,¹⁹⁴
 M. Antonova,⁸⁴ A. Antoshkin , A. Aranda-Fernandez,⁴² L. Arellano,¹³⁶ E. Arrieta Diaz,¹⁸¹
 M. A. Arroyave,⁶⁶ J. Asaadi,¹⁹⁸ A. Ashkenazi,¹⁹⁵ D. Asner,²⁰ L. Asquith,¹⁹² E. Atkin,⁸⁸
 D. Auguste,¹⁶¹ A. Aurisano,⁴⁰ V. Aushev,¹²⁵ D. Autiero,¹¹¹ M. B. Azam,⁸⁷ F. Azfar,¹⁵⁷
 A. Back,⁹¹ H. Back,¹⁵⁸ J. J. Back,²¹⁰ I. Bagaturia,⁷² L. Bagby,⁶⁶ N. Balashov ,
 S. Balasubramanian,⁶⁶ P. Baldi,²⁴ W. Baldini,⁹⁴ J. Baldonado,²⁰⁷ B. Baller,⁶⁶ B. Bambah,⁸²
 R. Banerjee,²¹⁷ F. Barao,^{128,113} D. Barbu,²¹ G. Barenboim,⁸⁴ P. Barham Alzás,³⁵
 G. J. Barker,²¹⁰ W. Barkhouse,¹⁴⁹ G. Barr,¹⁵⁷ J. Barranco Monarca,⁷⁷ A. Barros,¹⁹⁴
 N. Barros,^{128,61} D. Barrow,¹⁵⁷ J. L. Barrow,¹⁴⁴ A. Basharina-Freshville,²⁰⁴ A. Bashyal,⁸
 V. Basque,⁶⁶ C. Batchelor,⁵⁷ L. Bathe-Peters,¹⁵⁷ J.B.R. Battat,²¹¹ F. Battisti,¹⁵⁷ F. Bay,⁴
 M. C. Q. Bazetto,³⁰ J. L. L. Bazo Alba,¹⁷⁰ J. F. Beacom,¹⁵⁵ E. Bechetoille,¹¹¹ B. Behera,¹⁸⁷
 E. Belchior,¹³¹ G. Bell,⁵² L. Bellantoni,⁶⁶ G. Bellettini,^{103,168} V. Bellini,^{93,31} O. Beltramello,³⁵
 N. Benekos,³⁵ C. Benitez Montiel,^{84,10} D. Benjamin,²⁰ F. Bento Neves,¹²⁸ J. Berger,⁴⁴
 S. Berkman,¹⁴⁰ J. Bernal,¹⁰ P. Bernardini,^{97,180} A. Bersani,⁹⁶ S. Bertolucci,^{92,17}
 M. Betancourt,⁶⁶ A. Betancur Rodríguez,⁵⁸ A. Bevan,¹⁷³ Y. Bezawada,²³ A. T. Bezerra,⁶²
 T. J. Bezerra,¹⁹² A. Bhat,³⁷ V. Bhatnagar,¹⁶⁰ J. Bhatt,²⁰⁴ M. Bhattacharjee,⁸⁹
 M. Bhattacharya,⁶⁶ S. Bhuller,¹⁹ B. Bhuyan,⁸⁹ S. Biagi,¹⁰⁶ J. Bian,²⁴ K. Biery,⁶⁶
 B. Bilki,^{15,109} M. Bishai,²⁰ A. Bitadze,¹³⁶ A. Blake,¹²⁶ F. D. Blaszczyk,⁶⁶ G. C. Blazey,¹⁵⁰
 E. Blucher,³⁷ A. Bodek,¹⁷⁶ J. Bogenschuetz,¹⁹⁸ J. Boissevain,¹³⁰ S. Bolognesi,³⁴
 T. Bolton,¹²⁰ L. Bomben,^{98,108} M. Bonesini,^{98,141} C. Bonilla-Diaz,³² F. Bonini,²⁰ A. Booth,¹⁷³
 F. Boran,⁹¹ S. Bordini,³⁵ R. Borges Merlo,³⁰ A. Borkum,¹⁹² N. Bostan,¹⁰⁹ R. Bouet,¹³²
 J. Boza,⁴⁴ J. Bracinik,¹⁶ B. Brahma,⁹⁰ D. Brailsford,¹²⁶ F. Bramati,⁹⁸ A. Branca,⁹⁸
 A. Brandt,¹⁹⁸ J. Bremer,³⁵ C. Brew,¹⁷⁹ S. J. Brice,⁶⁶ V. Brio,⁹³ C. Brizzolari,^{98,141}
 C. Bromberg,¹⁴⁰ J. Brooke,¹⁹ A. Bross,⁶⁶ G. Brunetti,^{98,141} M. Brunetti,²¹⁰ N. Buchanan,⁴⁴
 H. Budd,¹⁷⁶ J. Buergi,¹⁴ A. Bundock,¹⁹ D. Burgardt,²¹² S. Butchart,¹⁹² G. Caceres V.,²³
 I. Cagnoli,^{92,17} T. Cai,²¹⁷ R. Calabrese,¹⁰⁰ R. Calabrese,^{94,67} J. Calcutt,^{20,156} L. Calivers,¹⁴

E. Calvo,³⁹ A. Caminata,⁹⁶ A. F. Camino,¹⁶⁹ W. Campanelli,¹²⁸ A. Campani,^{96,71}
A. Campos Benitez,²⁰⁸ N. Canci,¹⁰⁰ J. Capó,⁸⁴ I. Caracas,¹³⁵ D. Caratelli,²⁷ D. Carber,⁴⁴
J. M. Carceller,³⁵ G. Carini,²⁰ B. Carlus,¹¹¹ M. F. Carneiro,²⁰ P. Carniti,⁹⁸ I. Caro Terrazas,⁴⁴
H. Carranza,¹⁹⁸ N. Carrara,²³ L. Carroll,¹²⁰ T. Carroll,²¹⁴ A. Carter,¹⁷⁷ E. Casarejos,²⁰⁷
D. Casazza,⁹⁴ J. F. Castaño Forero,⁷ F. A. Castaño,⁶ A. Castillo,¹⁸³ C. Castromonte,¹⁰⁷
E. Catano-Mur,²¹³ C. Cattadori,⁹⁸ F. Cavalier,¹⁶¹ F. Cavanna,⁶⁶ S. Centro,¹⁵⁹ G. Cerati,⁶⁶
C. Cerna,¹³² A. Cervelli,⁹² A. Cervera Villanueva,⁸⁴ K. Chakraborty,¹⁶⁷ M. Chalifour,³⁵
A. Chappell,²¹⁰ N. Charitonidis,³⁵ A. Chatterjee,¹⁶⁷ H. Chen,²⁰ M. Chen,²⁴ W. C. Chen,²⁰⁰
Y. Chen,¹⁸⁵ Z. Chen-Wishart,¹⁷⁷ D. Cherdack,⁸¹ C. Chi,⁴⁵ F. Chiapponi,⁹² R. Chirco,⁸⁷
N. Chitirasreemadam,^{103,168} K. Cho,¹²³ S. Choate,¹⁰⁹ G. Choi,¹⁷⁶ D. Chokheli,⁷²
P. S. Chong,¹⁶⁵ B. Chowdhury,⁸ D. Christian,⁶⁶ A. Chukanov , M. Chung,²⁰³
E. Church,¹⁵⁸ M. F. Cicala,²⁰⁴ M. Cicerchia,¹⁵⁹ V. Cicero,^{92,17} R. Ciolini,¹⁰³ P. Clarke,⁵⁷
G. Cline,¹²⁷ T. E. Coan,¹⁸⁹ A. G. Cocco,¹⁰⁰ J. A. B. Coelho,¹⁶² A. Cohen,¹⁶² J. Collazo,²⁰⁷
J. Collot,⁷⁶ E. Conley,⁵⁵ J. M. Conrad,¹³⁷ M. Convery,¹⁸⁵ S. Copello,⁹⁶ P. Cova,^{99,163}
C. Cox,¹⁷⁷ L. Cremaldi,¹⁴⁵ L. Cremonesi,¹⁷³ J. I. Crespo-Anadón,³⁹ M. Crisler,⁶⁶
E. Cristaldo,^{98,10} J. Crnkovic,⁶⁶ G. Crone,²⁰⁴ R. Cross,²¹⁰ A. Cudd,⁴³ C. Cuesta,³⁹ Y. Cui,²⁶
F. Curciarello,⁹⁵ D. Cussans,¹⁹ J. Dai,⁷⁶ O. Dalager,⁶⁶ R. Dallavalle,¹⁶² W. Dallaway,²⁰⁰
R. D'Amico,^{94,67} H. da Motta,³³ Z. A. Dar,²¹³ R. Darby,¹⁹² L. Da Silva Peres,⁶⁵ Q. David,¹¹¹
G. S. Davies,¹⁴⁵ S. Davini,⁹⁶ J. Dawson,¹⁶² R. De Aguiar,³⁰ P. De Almeida,³⁰ P. Debbins,¹⁰⁹
I. De Bonis,⁵¹ M. P. Decowski,^{147,3} A. de Gouvêa,¹⁵¹ P. C. De Holanda,³⁰ I. L. De Icaza
Astiz,¹⁹² P. De Jong,^{147,3} P. Del Amo Sanchez,⁵¹ A. De la Torre,³⁹ G. De Lauretis,¹¹¹
A. Delbart,³⁴ D. Delepine,⁷⁷ M. Delgado,^{98,141} A. Dell'Acqua,³⁵ G. Delle Monache,⁹⁵
N. Delmonte,^{99,163} P. De Lurgio,⁸ R. Demario,¹⁴⁰ G. De Matteis,^{97,180} J. R. T. de Mello
Neto,⁶⁵ D. M. DeMuth,²⁰⁶ S. Dennis,²⁹ C. Densham,¹⁷⁹ P. Denton,²⁰ G. W. Deptuch,²⁰ A. De
Roeck,³⁵ V. De Romeri,⁸⁴ J. P. Detje,²⁹ J. Devine,³⁵ R. Dharmapalan,⁷⁹ M. Dias,²⁰²
A. Diaz,²⁸ J. S. Díaz,⁹¹ F. Díaz,¹⁷⁰ F. Di Capua,^{100,146} A. Di Domenico,^{182,104} S. Di
Domizio,^{96,71} S. Di Falco,¹⁰³ L. Di Giulio,³⁵ P. Ding,⁶⁶ L. Di Noto,^{96,71} E. Diociaiuti,⁹⁵
C. Distefano,¹⁰⁶ R. Diurba,¹⁴ M. Diwan,²⁰ Z. Djurcic,⁸ D. Doering,¹⁸⁵ S. Dolan,³⁵
F. Dolek,²⁰⁸ M. J. Dolinski,⁵⁴ D. Domenici,⁹⁵ L. Domine,¹⁸⁵ S. Donati,^{103,168} Y. Donon,³⁵
S. Doran,¹¹⁰ D. Douglas,¹⁸⁵ T.A. Doyle,¹⁹⁰ A. Dragone,¹⁸⁵ F. Drielsma,¹⁸⁵ L. Duarte,²⁰²
D. Duchesneau,⁵¹ K. Duffy,¹⁵⁷ K. Dugas,²⁴ P. Dunne,⁸⁸ B. Dutta,¹⁹⁶ H. Duyang,¹⁸⁶
D. A. Dwyer,¹²⁷ A. S. Dyshkant,¹⁵⁰ S. Dytman,¹⁶⁹ M. Eads,¹⁵⁰ A. Earle,¹⁹² S. Edayath,¹¹⁰
D. Edmunds,¹⁴⁰ J. Eisch,⁶⁶ P. Englezos,¹⁷⁸ A. Ereditato,³⁷ T. Erjavec,²³ C. O. Escobar,⁶⁶
J. J. Evans,¹³⁶ E. Ewart,⁹¹ A. C. Ezeribe,¹⁸⁴ K. Fahey,⁶⁶ L. Fajt,³⁵ A. Falcone,^{98,141}
M. Fani,^{144,130} C. Farnese,¹⁰¹ S. Farrell,¹⁷⁵ Y. Farzan,¹¹² D. Fedoseev , J. Felix,⁷⁷
Y. Feng,¹¹⁰ E. Fernandez-Martinez,¹³⁴ G. Ferry,¹⁶¹ E. Fialova,⁵⁰ L. Fields,¹⁵² P. Filip,⁴⁹
A. Filkins,¹⁹³ F. Filthaut,^{147,174} R. Fine,¹³⁰ G. Fiorillo,^{100,146} M. Fiorini,^{94,67} S. Fogarty,⁴⁴
W. Foreman,¹³⁰ J. Fowler,⁵⁵ J. Franc,⁵⁰ K. Francis,¹⁵⁰ D. Franco,³⁷ J. Franklin,⁵⁶
J. Freeman,⁶⁶ J. Fried,²⁰ A. Friedland,¹⁸⁵ S. Fuess,⁶⁶ I. K. Furic,⁶⁸ K. Furman,¹⁷³
A. P. Furmanski,¹⁴⁴ R. Gaba,¹⁶⁰ A. Gabrielli,^{92,17} A. M Gago,¹⁷⁰ F. Galizzi,⁹⁸ H. Gallagher,²⁰¹
N. Gallice,²⁰ V. Galymov,¹¹¹ E. Gamberini,³⁵ T. Gamble,¹⁸⁴ F. Ganacim,¹⁹⁴ R. Gandhi,⁷⁸
S. Ganguly,⁶⁶ F. Gao,²⁷ S. Gao,²⁰ D. Garcia-Gamez,⁷³ M. Á. García-Peris,¹³⁶ F. Gardim,⁶²
S. Gardiner,⁶⁶ D. Gastler,¹⁸ A. Gauch,¹⁴ J. Gauvreau,¹⁵⁴ P. Gauzzi,^{182,104} S. Gazzana,⁹⁵

G. Ge,⁴⁵ N. Geffroy,⁵¹ B. Gelli,³⁰ S. Gent,¹⁸⁸ L. Gerlach,²⁰ Z. Ghorbani-Moghaddam,⁹⁶
 T. Giammaria,^{94,67} D. Gibin,^{159,101} I. Gil-Botella,³⁹ S. Gilligan,¹⁵⁶ A. Gioiosa,¹⁰⁵
 S. Giovannella,⁹⁵ C. Girerd,¹¹¹ A. K. Giri,⁹⁰ C. Giugliano,⁹⁴ V. Giusti,¹⁰³ D. Gnani,¹²⁷
 O. Gogota,¹²⁵ S. Gollapinni,¹³⁰ K. Gollwitzer,⁶⁶ R. A. Gomes,⁶³ L. V. Gomez Bermeo,¹⁸³
 L. S. Gomez Fajardo,¹⁸³ F. Gonnella,¹⁶ D. Gonzalez-Diaz,⁸⁵ M. Gonzalez-Lopez,¹³⁴
 M. C. Goodman,⁸ S. Goswami,¹⁶⁷ C. Gotti,⁹⁸ J. Goudeau,¹³¹ E. Goudzovski,¹⁶ C. Grace,¹²⁷
 E. Gramellini,¹³⁶ R. Gran,¹⁴³ E. Granados,⁷⁷ P. Granger,¹⁶² C. Grant,¹⁸ D. R. Gratieri,^{70,30}
 G. Grauso,¹⁰⁰ P. Green,¹⁵⁷ S. Greenberg,^{127,22} J. Greer,¹⁹ W. C. Griffith,¹⁹²
 F. T. Groetschla,³⁵ K. Grzelak,²⁰⁹ L. Gu,¹²⁶ W. Gu,²⁰ V. Guarino,⁸ M. Guarise,^{94,67}
 R. Guenette,¹³⁶ M. Guerzoni,⁹² D. Guffanti,^{98,141} A. Guglielmi,¹⁰¹ B. Guo,¹⁸⁶ F. Y. Guo,¹⁹⁰
 A. Gupta,¹⁸⁵ V. Gupta,^{147,3} G. Gurung,¹⁹⁸ D. Gutierrez,¹⁷¹ P. Guzowski,¹³⁶ M. M. Guzzo,³⁰
 S. Gwon,³⁸ A. Habig,¹⁴³ H. Hadavand,¹⁹⁸ L. Haegel,¹¹¹ R. Haenni,¹⁴ L. Hagaman,²¹⁵
 A. Hahn,⁶⁶ J. Haiston,¹⁸⁷ J. Hakenmüller,⁵⁵ T. Hamernik,⁶⁶ P. Hamilton,⁸⁸ J. Hancock,¹⁶
 F. Happacher,⁹⁵ D. A. Harris,^{217,66} A. L. Hart,¹⁷³ J. Hartnell,¹⁹² T. Hartnett,¹⁷⁹ J. Harton,⁴⁴
 T. Hasegawa,¹²² C. M. Hasnip,³⁵ R. Hatcher,⁶⁶ K. Hayrapetyan,¹⁷³ J. Hays,¹⁷³ E. Hazen,¹⁸
 M. He,⁸¹ A. Heavey,⁶⁶ K. M. Heeger,²¹⁵ J. Heise,¹⁹¹ P. Hellmuth,¹³² S. Henry,¹⁷⁶ K. Herner,⁶⁶
 V. Hewes,⁴⁰ A. Higuera,¹⁷⁵ C. Hilgenberg,¹⁴⁴ S. J. Hillier,¹⁶ A. Himmel,⁶⁶ E. Hinkle,³⁷
 L.R. Hirsch,¹⁹⁴ J. Ho,⁵³ J. Hoff,⁶⁶ A. Holin,¹⁷⁹ T. Holvey,¹⁵⁷ E. Hoppe,¹⁵⁸ S. Horiuchi,²⁰⁸
 G. A. Horton-Smith,¹²⁰ T. Houdy,¹⁶¹ B. Howard,^{217,66} R. Howell,¹⁷⁶ I. Hristova,¹⁷⁹
 M. S. Hronek,⁶⁶ J. Huang,²³ R.G. Huang,¹²⁷ Z. Hulcher,¹⁸⁵ M. Ibrahim,⁵⁹ G. Iles,⁸⁸ N. Ilic,²⁰⁰
 A. M. Iliescu,⁹⁵ R. Illingworth,⁶⁶ G. Ingratta,^{92,17} A. Ioannisian,²¹⁶ B. Irwin,¹⁴⁴
 L. Isenhowe,⁰ M. Ismerio Oliveira,⁶⁵ R. Itay,¹⁸⁵ C.M. Jackson,¹⁵⁸ V. Jain,¹ E. James,⁶⁶
 W. Jang,¹⁹⁸ B. Jargowsky,²⁴ D. Jena,⁶⁶ I. Jentz,²¹⁴ X. Ji,²⁰ C. Jiang,¹¹⁶ J. Jiang,¹⁹⁰
 L. Jiang,²⁰⁸ A. Jipa,²¹ J. H. Jo,²⁰ F. R. Joaquim,^{128,113} W. Johnson,¹⁸⁷ C. Jollet,¹³²
 B. Jones,¹⁹⁸ R. Jones,¹⁸⁴ N. Jovancevic,¹⁵³ M. Judah,¹⁶⁹ C. K. Jung,¹⁹⁰ K. Y. Jung,¹⁷⁶
 T. Junk,⁶⁶ Y. Jwa,^{185,45} M. Kabirnezhad,⁸⁸ A. C. Kaboth,^{177,179} I. Kadenko,¹²⁵ I. Kakorin ,
 A. Kalitkina , D. Kalra,⁴⁵ M. Kandemir,⁶⁰ D. M. Kaplan,⁸⁷ G. Karagiorgi,⁴⁵ G. Karaman,¹⁰⁹
 A. Karcher,¹²⁷ Y. Karyotakis,⁵¹ S. Kasai,¹²⁴ S. P. Kasetti,¹³¹ L. Kashur,⁴⁴ I. Katsioulas,¹⁶
 A. Kauther,¹⁵⁰ N. Kazaryan,²¹⁶ L. Ke,²⁰ E. Kearns,¹⁸ P.T. Keener,¹⁶⁵ K.J. Kelly,¹⁹⁶
 E. Kemp,³⁰ O. Kemularia,⁷² Y. Kermaidic,¹⁶¹ W. Ketchum,⁶⁶ S. H. Kettell,²⁰
 M. Khabibullin , N. Khan,⁸⁸ A. Khvedelidze,⁷² D. Kim,¹⁹⁶ J. Kim,¹⁷⁶ M. J. Kim,⁶⁶
 B. King,⁶⁶ B. Kirby,⁴⁵ M. Kirby,²⁰ A. Kish,⁶⁶ J. Klein,¹⁶⁵ J. Kleykamp,¹⁴⁵ A. Klustova,⁸⁸
 T. Kobilarcik,⁶⁶ L. Koch,¹³⁵ K. Koehler,²¹⁴ L. W. Koerner,⁸¹ D. H. Koh,¹⁸⁵ L. Kolupaeva ,
 D. Korablev , M. Kordosky,²¹³ T. Kosc,⁷⁶ U. Kose,³⁵ V. A. Kostelecký,⁹¹ K. Kotheke,¹⁹
 I. Kotler,⁵⁴ M. Kovalcuk,⁴⁹ V. Kozhukalov , W. Krah,¹⁴⁷ R. Kralik,¹⁹² M. Kramer,¹²⁷
 L. Kreczko,¹⁹ F. Krennrich,¹¹⁰ I. Kreslo,¹⁴ T. Kroupova,¹⁶⁵ S. Kubota,¹³⁶ M. Kubu,³⁵
 Y. Kudenko , V. A. Kudryavtsev,¹⁸⁴ G. Kufatty,⁶⁹ S. Kuhlmann,⁸ S. Kulagin , J. Kumar,⁷⁹
 P. Kumar,¹⁸⁴ S. Kumaran,²⁴ J. Kunzmann,¹⁴ R. Kuravi,¹²⁷ N. Kurita,¹⁸⁵ C. Kuruppu,¹⁸⁶
 V. Kus,⁵⁰ T. Kutter,¹³¹ J. Kvasnicka,⁴⁹ T. Labree,¹⁵⁰ T. Lackey,⁶⁶ I. Lalău,²¹ A. Lambert,¹²⁷
 B. J. Land,¹⁶⁵ C. E. Lane,⁵⁴ N. Lane,¹³⁶ K. Lang,¹⁹⁹ T. Langford,²¹⁵ M. Langstaff,¹³⁶
 F. Lanni,³⁵ O. Lantwin,⁵¹ J. Larkin,²⁰ P. Lasorak,⁸⁸ D. Last,¹⁶⁵ A. Laudrain,¹³⁵
 A. Landrie,²¹⁴ G. Laurenti,⁹² E. Lavaut,¹⁶¹ P. Laycock,²⁰ I. Lazanu,²¹ R. LaZur,⁴⁴
 M. Lazzaroni,^{99,142} T. Le,²⁰¹ S. Leardini,⁸⁵ J. Learned,⁷⁹ T. LeCompte,¹⁸⁵ V. Legin,¹²⁵

G. Lehmann Miotto,³⁵ R. Lehnert,⁹¹ M. A. Leigui de Oliveira,⁶⁴ M. Leitner,¹²⁷ D. Leon Silverio,¹⁸⁷ L. M. Lepin,⁶⁹ J.-Y Li,⁵⁷ S. W. Li,²⁴ Y. Li,²⁰ H. Liao,¹²⁰ C. S. Lin,¹²⁷ D. Lindebaum,¹⁹ S. Linden,²⁰ R. A. Lineros,³² A. Lister,²¹⁴ B. R. Littlejohn,⁸⁷ H. Liu,²⁰ J. Liu,²⁴ Y. Liu,³⁷ S. Lockwitz,⁶⁶ M. Lokajicek,⁴⁹ I. Lomidze,⁷² K. Long,⁸⁸ T. V. Lopes,⁶² J. Lopez,⁶ I. López de Rego,³⁹ N. López-March,⁸⁴ T. Lord,²¹⁰ J. M. LoSecco,¹⁵² W. C. Louis,¹³⁰ A. Lozano Sanchez,⁵⁴ X.-G. Lu,²¹⁰ K.B. Luk,^{80,127,22} B. Lunday,¹⁶⁵ X. Luo,²⁷ E. Luppi,^{94,67} D. MacFarlane,¹⁸⁵ A. A. Machado,³⁰ P. Machado,⁶⁶ C. T. Macias,⁹¹ J. R. Macier,⁶⁶ M. MacMahon,²⁰⁴ A. Maddalena,⁷⁵ A. Madera,³⁵ P. Madigan,^{22,127} S. Magill,⁸ C. Magueur,¹⁶¹ K. Mahn,¹⁴⁰ A. Maio,^{128,61} A. Major,⁵⁵ K. Majumdar,¹²⁹ S. Mamelí,¹⁰³ M. Man,²⁰⁰ R. C. Mandujano,²⁴ J. Maneira,^{128,61} S. Manly,¹⁷⁶ A. Mann,²⁰¹ K. Manolopoulos,¹⁷⁹ M. Manrique Plata,⁹¹ S. Manthey Corchado,³⁹ V. N. Manyam,²⁰ M. Marchan,⁶⁶ A. Marchionni,⁶⁶ W. Marciano,²⁰ D. Marfatia,⁷⁹ C. Mariani,²⁰⁸ J. Maricic,⁷⁹ F. Marinho,¹¹⁴ A. D. Marino,⁴³ T. Markiewicz,¹⁸⁵ F. Das Chagas Marques,³⁰ C. Marquet,¹³² M. Marshak,¹⁴⁴ C. M. Marshall,¹⁷⁶ J. Marshall,²¹⁰ L. Martina,^{97,180} J. Martín-Albo,⁸⁴ N. Martinez,¹²⁰ D.A. Martinez Caicedo,¹⁸⁷ F. Martínez López,¹⁷³ P. Martínez Miravé,⁸⁴ S. Martynenko,²⁰ V. Mascagna,⁹⁸ C. Massari,⁹⁸ A. Mastbaum,¹⁷⁸ F. Matichard,¹²⁷ S. Matsuno,⁷⁹ G. Matteucci,^{100,146} J. Matthews,¹³¹ C. Mauger,¹⁶⁵ N. Mauri,^{92,17} K. Mavrokoridis,¹²⁹ I. Mawby,¹²⁶ R. Mazza,⁹⁸ T. McAskill,²¹¹ N. McConkey,^{173,204} K. S. McFarland,¹⁷⁶ C. McGrew,¹⁹⁰ A. McNab,¹³⁶ L. Meazza,⁹⁸ V. C. N. Meddage,⁶⁸ A. Mefodiev,¹⁶ B. Mehta,¹⁶⁰ P. Mehta,¹¹⁷ P. Melas,¹¹ O. Mena,⁸⁴ H. Mendez,¹⁷¹ P. Mendez,³⁵ D. P. Méndez,²⁰ A. Menegolli,^{102,164} G. Meng,¹⁰¹ A. C. E. A. Mercuri,¹⁹⁴ A. Meregaglia,¹³² M. D. Messier,⁹¹ S. Metallo,¹⁴⁴ W. Metcalf,¹³¹ M. Mewes,⁹¹ H. Meyer,²¹² T. Miao,⁶⁶ J. Micallef,^{201,137} A. Miccoli,⁹⁷ G. Michna,¹⁸⁸ R. Milincic,⁷⁹ F. Miller,²¹⁴ G. Miller,¹³⁶ W. Miller,¹⁴⁴ O. Mineev,¹⁶ A. Minotti,^{98,141} L. Miralles,³⁵ C. Mironov,¹⁶² S. Miryala,²⁰ S. Miscetti,⁹⁵ C. S. Mishra,⁶⁶ P. Mishra,⁸² S. R. Mishra,¹⁸⁶ A. Mislivec,¹⁴⁴ M. Mitchell,¹³¹ D. Mladenov,³⁵ I. Mocioiu,¹⁶⁶ A. Mogan,⁶⁶ N. Moggi,^{92,17} R. Mohanta,⁸² T. A. Mohayai,⁹¹ N. Mokhov,⁶⁶ J. Molina,¹⁰ L. Molina Bueno,⁸⁴ E. Montagna,^{92,17} A. Montanari,⁹² C. Montanari,^{102,66,164} D. Montanari,⁶⁶ D. Montanino,^{97,180} L. M. Montaña Zetina,⁴¹ M. Mooney,⁴⁴ A. F. Moor,¹⁸⁴ Z. Moore,¹⁹³ D. Moreno,⁷ O. Moreno-Palacios,²¹³ L. Morescalchi,¹⁰³ D. Moretti,⁹⁸ R. Moretti,⁹⁸ C. Morris,⁸¹ C. Mossey,⁶⁶ C. A. Moura,⁶⁴ G. Mouser,¹²⁶ W. Mu,⁶⁶ L. Mualem,²⁸ J. Mueller,⁴⁴ M. Muether,²¹² F. Muheim,⁵⁷ A. Muir,⁵² Y. Mukhamejanov,² M. Mulhearn,²³ D. Munford,⁸¹ L. J. Munteanu,³⁵ H. Muramatsu,¹⁴⁴ J. Muraz,⁷⁶ M. Murphy,²⁰⁸ T. Murphy,¹⁹³ J. Muse,¹⁴⁴ A. Mytilinaki,¹⁷⁹ J. Nachtman,¹⁰⁹ Y. Nagai,⁵⁹ S. Nagu,¹³³ R. Nandakumar,¹⁷⁹ D. Naples,¹⁶⁹ S. Narita,¹¹⁵ A. Navrer-Agasson,^{88,136} N. Nayak,²⁰ M. Nebot-Guinet,⁵⁷ A. Nehm,¹³⁵ J. K. Nelson,²¹³ O. Neogi,¹⁰⁹ J. Nesbit,²¹⁴ M. Nessi,^{66,35} D. Newbold,¹⁷⁹ M. Newcomer,¹⁶⁵ R. Nichol,²⁰⁴ F. Nicolas-Arnaldos,⁷³ A. Nikolica,¹⁶⁵ J. Nikolov,¹⁵³ E. Niner,⁶⁶ K. Nishimura,⁷⁹ A. Norman,⁶⁶ A. Norrick,⁶⁶ P. Novella,⁸⁴ A. Nowak,¹²⁶ J. A. Nowak,¹²⁶ M. Oberling,⁸ J. P. Ochoa-Ricoux,²⁴ S. Oh,⁵⁵ S.B. Oh,⁶⁶ A. Olivier,¹⁵² A. Olshevskiy,¹⁶ T. Olson,⁸¹ Y. Onel,¹⁰⁹ Y. Onishchuk,¹²⁵ A. Oranday,⁹¹ M. Osbiston,²¹⁰ J. A. Osorio Vélez,⁶ L. O'Sullivan,¹³⁵ L. Otiniano Ormachea,^{46,107} J. Ott,²⁴ L. Pagani,²³ G. Palacio,⁵⁸ O. Palamara,⁶⁶ S. Palestini,³⁵ J. M. Paley,⁶⁶ M. Pallavicini,^{96,71} C. Palomares,³⁹ S. Pan,¹⁶⁷ P. Panda,⁸² W. Panduro Vazquez,¹⁷⁷ E. Pantic,²³ V. Paolone,¹⁶⁹ R. Papaleo,¹⁰⁶

A. Papanestis,¹⁷⁹ D. Papoulias,¹¹ S. Paramesvaran,¹⁹ A. Paris,¹⁷¹ S. Parke,⁶⁶
E. Parozzi,^{98,141} S. Parsa,¹⁴ Z. Parsa,²⁰ S. Parveen,¹¹⁷ M. Parvu,²¹ D. Pasciuto,¹⁰³
S. Pascoli,^{92,17} L. Pasqualini,^{92,17} J. Pasternak,⁸⁸ C. Patrick,^{57,204} L. Patrizii,⁹²
R. B. Patterson,²⁸ T. Patzak,¹⁶² A. Paudel,⁶⁶ L. Paulucci,⁶⁴ Z. Pavlovic,⁶⁶ G. Pawloski,¹⁴⁴
D. Payne,¹²⁹ V. Pec,⁴⁹ E. Pedreschi,¹⁰³ S. J. M. Peeters,¹⁹² W. Pellico,⁶⁶ A. Pena Perez,¹⁸⁵
E. Pennacchio,¹¹¹ A. Penzo,¹⁰⁹ O. L. G. Peres,³⁰ Y. F. Perez Gonzalez,⁵⁶ L. Pérez-Molina,³⁹
C. Pernas,²¹³ J. Perry,⁵⁷ D. Pershey,⁶⁹ G. Pessina,⁹⁸ G. Petrillo,¹⁸⁵ C. Petta,^{93,31} R. Petti,¹⁸⁶
M. Pfaff,⁸⁸ V. Pia,^{92,17} L. Pickering,^{179,177} F. Pietropaolo,^{35,101} V.L.Pimentel,^{47,30}
G. Pinaroli,²⁰ S. Pincha,⁸⁹ J. Pinchault,⁵¹ K. Pitts,²⁰⁸ K. Plows,¹⁵⁷ C. Pollack,¹⁷¹
T. Pollman,^{147,3} F. Pompa,⁸⁴ X. Pons,³⁵ N. Poonthottathil,^{86,110} V. Popov,¹⁹⁵ F. Poppi,^{92,17}
J. Porter,¹⁹² L. G. Porto Paixão,³⁰ M. Potekhin,²⁰ R. Potenza,^{93,31} M. Pozzato,^{92,17}
T. Prakash,¹²⁷ C. Pratt,²³ M. Prest,⁹⁸ F. Psihas,⁶⁶ D. Pugnere,¹¹¹ X. Qian,²⁰ J. Queen,⁵⁵
J. L. Raaf,⁶⁶ V. Radeka,²⁰ J. Rademacker,¹⁹ B. Radics,²¹⁷ F. Raffaelli,¹⁰³ A. Rafique,⁸
E. Raguzin,²⁰ U. Rahaman,²⁰⁰ M. Rai,²¹⁰ S. Rajagopalan,²⁰ M. Rajaoalisoa,⁴⁰ I. Rakhno,⁶⁶
L. Rakotondravohitra,⁵ L. Ralte,⁹⁰ M. A. Ramirez Delgado,¹⁶⁵ B. Ramson,⁶⁶
A. Rappoldi,^{102,164} G. Raselli,^{102,164} P. Ratoff,¹²⁶ R. Ray,⁶⁶ H. Razafinime,⁴⁰
R. F. Razakamiandra,¹⁹⁰ E. M. Rea,¹⁴⁴ J. S. Real,⁷⁶ B. Rebel,^{214,66} R. Rechenmacher,⁶⁶
J. Reichenbacher,¹⁸⁷ S. D. Reitzner,⁶⁶ H. Rejeb Sfar,³⁵ E. Renner,¹³⁰ A. Renshaw,⁸¹
S. Rescia,²⁰ F. Resnati,³⁵ Diego Restrepo,⁶ C. Reynolds,¹⁷³ M. Ribas,¹⁹⁴ S. Riboldi,⁹⁹
C. Riccio,¹⁹⁰ G. Riccobene,¹⁰⁶ J. S. Ricol,⁷⁶ M. Rigan,¹⁹² E. V. Rincón,⁵⁸
A. Ritchie-Yates,¹⁷⁷ S. Ritter,¹³⁵ D. Rivera,¹³⁰ R. Rivera,⁶⁶ A. Robert,⁷⁶ J. L. Rocabado
Rocha,⁸⁴ L. Rochester,¹⁸⁵ M. Roda,¹²⁹ P. Rodrigues,¹⁵⁷ M. J. Rodriguez Alonso,³⁵
J. Rodriguez Rondon,¹⁸⁷ S. Rosauero-Alcaraz,¹⁶¹ P. Rosier,¹⁶¹ D. Ross,¹⁴⁰
M. Rossella,^{102,164} M. Rossi,³⁵ M. Ross-Lonergan,¹³⁰ N. Roy,²¹⁷ P. Roy,²¹² C. Rubbia,⁷⁴
A. Ruggeri,⁹² G. Ruiz Ferreira,¹³⁶ B. Russell,¹³⁷ D. Ruterbories,¹⁷⁶ A. Rybnikov ,
S. Sacerdoti,¹⁶² S. Saha,¹⁶⁹ S. K. Sahoo,⁹⁰ N. Sahu,⁹⁰ P. Sala,⁶⁶ N. Samios,²⁰
O. Samoylov , M. C. Sanchez,⁶⁹ A. Sánchez Bravo,⁸⁴ A. Sánchez-Castillo,⁷³
P. Sanchez-Lucas,⁷³ V. Sandberg,¹³⁰ D. A. Sanders,¹⁴⁵ S. Sanfilippo,¹⁰⁶ D. Sankey,¹⁷⁹
D. Santoro,^{99,163} N. Saoulidou,¹¹ P. Sapienza,¹⁰⁶ C. Sarasty,⁴⁰ I. Sarcevic,⁹ I. Sarra,⁹⁵
G. Savage,⁶⁶ V. Savinov,¹⁶⁹ G. Scanavini,²¹⁵ A. Scaramelli,¹⁰² A. Scarff,¹⁸⁴ T. Schefke,¹³¹
H. Schellman,^{156,66} S. Schifano,^{94,67} P. Schlabach,⁶⁶ D. Schmitz,³⁷ A. W. Schneider,¹³⁷
K. Scholberg,⁵⁵ A. Schukraft,⁶⁶ B. Schuld,⁴³ A. Segade,²⁰⁷ E. Segreto,³⁰ A. Selyunin ,
A. Selyunin,¹⁴ D. Senadheera,¹⁶⁹ C. R. Senise,²⁰² J. Sensenig,¹⁶⁵ M. H. Shaevitz,⁴⁵
P. Shanahan,⁶⁶ P. Sharma,¹⁶⁰ R. Kumar,¹⁷² S. Sharma Poudel,¹⁸⁷ K. Shaw,¹⁹² T. Shaw,⁶⁶
K. Shchablo,¹¹¹ J. Shen,¹⁶⁵ C. Shepherd-Themistocleous,¹⁷⁹ A. Sheshukov , J. Shi,²⁹
W. Shi,¹⁹⁰ S. Shin,¹¹⁸ S. Shivakoti,²¹² I. Shoemaker,²⁰⁸ D. Shooltz,¹⁴⁰ R. Shrock,¹⁹⁰
B. Siddi,⁹⁴ M. Siden,⁴⁴ J. Silber,¹²⁷ L. Simard,¹⁶¹ J. Sinclair,¹⁸⁵ G. Sinev,¹⁸⁷ Jaydip Singh,²³
J. Singh,¹³³ L. Singh,⁴⁸ P. Singh,¹⁷³ V. Singh,⁴⁸ S. Singh Chauhan,¹⁶⁰ R. Sipos,³⁵
C. Sironneau,¹⁶² G. Sirri,⁹² K. Siyeon,³⁸ K. Skarpaas,¹⁸⁵ J. Smedley,¹⁷⁶ E. Smith,⁹¹
J. Smith,¹⁹⁰ P. Smith,⁹¹ J. Smolik,^{50,49} M. Smy,²⁴ M. Snape,²¹⁰ E.L. Snider,⁶⁶ P. Snopok,⁸⁷
D. Snowden-Ifft,¹⁵⁴ M. Soares Nunes,⁶⁶ H. Sobel,²⁴ M. Soderberg,¹⁹³ S. Sokolov ,
C. J. Solano Salinas,²⁰⁵ S. Söldner-Rembold,^{88,136} N. Solomey,²¹² V. Solovov,¹²⁸
W. E. Sondheim,¹³⁰ M. Sorel,⁸⁴ A. Sotnikov , J. Soto-Oton,⁸⁴ A. Sousa,⁴⁰

K. Soustruznik,³⁶ F. Spinella,¹⁰³ J. Spitz,¹³⁹ N. J. C. Spooner,¹⁸⁴ K. Spurgeon,¹⁹³
 D. Stalder,¹⁰ M. Stancari,⁶⁶ L. Stanco,^{159,101} J. Steenis,²³ R. Stein,¹⁹ H. M. Steiner,¹²⁷
 A. F. Steklain Lisbôa,¹⁹⁴ A. Stepanova , J. Stewart,²⁰ B. Stillwell,³⁷ J. Stock,¹⁸⁷
 F. Stocker,³⁵ T. Stokes,¹³¹ M. Strait,¹⁴⁴ T. Strauss,⁶⁶ L. Strigari,¹⁹⁶ A. Stuart,⁴²
 J. G. Suarez,⁵⁸ J. Subash,¹⁶ A. Surdo,⁹⁷ L. Suter,⁶⁶ C. M. Suter, ^{93,31} K. Sutton,²⁸
 Y. Suvorov,^{100,146} R. Svoboda,²³ S. K. Swain,¹⁴⁸ B. Szczerbinska,¹⁹⁷ A. M. Szelc,⁵⁷
 A. Sztuc,²⁰⁴ A. Taffara,¹⁰³ N. Talukdar,¹⁸⁶ J. Tamara,⁷ H. A. Tanaka,¹⁸⁵ S. Tang,²⁰
 N. Taniuchi,²⁹ A. M. Tapia Casanova,¹³⁸ B. Tapia Oregui,¹⁹⁹ A. Tapper,⁸⁸ S. Tariq,⁶⁶
 E. Tarpara,²⁰ E. Tatar,⁸³ R. Tayloe,⁹¹ D. Tedeschi,¹⁸⁶ A. M. Teklu,¹⁹⁰ J. Tena Vidal,¹⁹⁵
 P. Tennessen,^{127,4} M. Tenti,⁹² K. Terao,¹⁸⁵ F. Terranova,^{98,141} G. Testera,⁹⁶ T. Thakore,⁴⁰
 A. Thea,¹⁷⁹ S. Thomas,¹⁹³ A. Thompson,¹⁵¹ C. Thorn,²⁰ S. C. Timm,⁶⁶ E. Tiras,^{60,109}
 V. Tishchenko,²⁰ S. Tiwari,¹⁷⁶ N. Todorović,¹⁵³ L. Tomassetti,^{94,67} A. Tonazzo,¹⁶²
 D. Torbunov,²⁰ M. Torti,^{98,141} M. Tortola,⁸⁴ F. Tortorici,^{93,31} N. Tosi,⁹² D. Totani,²⁷
 M. Touns,⁶⁶ C. Touramanis,¹²⁹ D. Tran,⁸¹ R. Travaglini,⁹² J. Trevor,²⁸ E. Triller,¹⁴⁰
 S. Trilov,¹⁹ J. Truchon,²¹⁴ D. Truncali,^{182,104} W. H. Trzaska,¹¹⁹ Y. Tsai,²⁴ Y.-T. Tsai,¹⁸⁵
 Z. Tsamalaidze,⁷² K. V. Tsang,¹⁸⁵ N. Tserava,⁷² S. Z. Tu,¹¹⁶ S. Tufanli,³⁵ C. Tunnell,¹⁷⁵
 S. Turnberg,⁸⁷ J. Turner,⁵⁶ M. Tuzi,⁸⁴ J. Tyler,¹²⁰ E. Tyley,¹⁸⁴ M. Tzanov,¹³¹ M. A. Uchida,²⁹
 J. Ureña González,⁸⁴ J. Urheim,⁹¹ T. Usher,¹⁸⁵ H. Utaegbulam,¹⁷⁶ S. Uzunyan,¹⁵⁰
 M. R. Vagins,^{121,24} P. Vahle,²¹³ S. Valder,¹⁹² G. A. Valdivieso,⁶² E. Valencia,⁷⁷
 R. Valentim,²⁰² Z. Vallari,²⁸ E. Vallazza,⁹⁸ J. W. F. Valle,⁸⁴ R. Van Berg,¹⁶⁵ R. G. Van de
 Water,¹³⁰ D. V. Forero,¹³⁸ A. Vannozzi,⁹⁵ M. Van Nuland-Troost,¹⁴⁷ F. Varanini,¹⁰¹
 D. Vargas Oliva,²⁰⁰ S. Vasina , N. Vaughan,¹⁵⁶ K. Vaziri,⁶⁶ A. Vázquez-Ramos,⁷³
 J. Vega,⁴⁶ S. Ventura,¹⁰¹ A. Verdugo,³⁹ S. Vergani,²⁰⁴ M. Verzocchi,⁶⁶ K. Vetter,⁶⁶
 M. Vicenzi,²⁰ H. Vieira de Souza,¹⁶² C. Vignoli,⁷⁵ C. Vilela,¹²⁸ E. Villa,³⁵ S. Viola,¹⁰⁶
 B. Viren,²⁰ R. Vizarreta,¹⁷⁶ A. P. Vizcaya Hernandez,⁴⁴ Q. Vuong,¹⁷⁶ A. V. Waldron,¹⁷³
 M. Wallbank,⁴⁰ J. Walsh,¹⁴⁰ T. Walton,⁶⁶ H. Wang,²⁵ J. Wang,¹⁸⁷ L. Wang,¹²⁷
 M.H.L.S. Wang,⁶⁶ X. Wang,⁶⁶ Y. Wang,²⁵ K. Warburton,¹¹⁰ D. Warner,⁴⁴ L. Warsame,⁸⁸
 M.O. Wascko,^{157,179} D. Waters,²⁰⁴ A. Watson,¹⁶ K. Wawrowska,^{179,192} A. Weber,^{135,66}
 C. M. Weber,¹⁴⁴ M. Weber,¹⁴ H. Wei,¹³¹ A. Weinstein,¹¹⁰ S. Westerdale,²⁶ M. Wetstein,¹¹⁰
 K. Whalen,¹⁷⁹ A. White,¹⁹⁸ A. White,²¹⁵ L. H. Whitehead,²⁹ D. Whittington,¹⁹³
 J. Wilhlemi,²¹⁵ M. J. Wilking,¹⁴⁴ A. Wilkinson,²⁰⁴ C. Wilkinson,¹²⁷ F. Wilson,¹⁷⁹
 R. J. Wilson,⁴⁴ P. Winter,⁸ W. Wisniewski,¹⁸⁵ J. Wolcott,²⁰¹ J. Wolfs,¹⁷⁶ T. Wongjirad,²⁰¹
 A. Wood,⁸¹ K. Wood,¹²⁷ E. Worcester,²⁰ M. Worcester,²⁰ M. Wospakrik,⁶⁶ K. Wresilo,²⁹
 C. Wret,¹⁷⁶ S. Wu,¹⁴⁴ W. Wu,⁶⁶ W. Wu,²⁴ M. Wurm,¹³⁵ J. Wyenberg,⁵³ Y. Xiao,²⁴ I. Xiotidis,⁸⁸
 B. Yaeggy,⁴⁰ N. Yahlali,⁸⁴ E. Yandel,²⁷ J. Yang,⁸⁰ K. Yang,¹⁵⁷ T. Yang,⁶⁶ A. Yankelevich,²⁴
 N. Yershov , K. Yonehara,⁶⁶ T. Young,¹⁴⁹ B. Yu,²⁰ H. Yu,²⁰ J. Yu,¹⁹⁸ Y. Yu,⁸⁷ W. Yuan,⁵⁷
 R. Zaki,²¹⁷ J. Zalesak,⁴⁹ L. Zambelli,⁵¹ B. Zamorano,⁷³ A. Zani,⁹⁹ O. Zapata,⁶ L. Zazueta,¹⁹³
 G. P. Zeller,⁶⁶ J. Zennamo,⁶⁶ K. Zeug,²¹⁴ C. Zhang,²⁰ S. Zhang,⁹¹ M. Zhao,²⁰ E. Zhivun,²⁰
 E. D. Zimmerman,⁴³ S. Zucchelli,^{92,17} J. Zuklin,⁴⁹ V. Zutshi,¹⁵⁰ and R. Zwaska⁶⁶

⁰Abilene Christian University, Abilene, TX 79601, USA

¹University of Albany, SUNY, Albany, NY 12222, USA

²Institute of Nuclear Physics at Almaty, Almaty 050032, Kazakhstan

³University of Amsterdam, NL-1098 XG Amsterdam, The Netherlands

- ⁴*Antalya Bilim University, 07190 Döşemealtı/Antalya, Turkey*
- ⁵*University of Antananarivo, Antananarivo 101, Madagascar*
- ⁶*University of Antioquia, Medellín, Colombia*
- ⁷*Universidad Antonio Nariño, Bogotá, Colombia*
- ⁸*Argonne National Laboratory, Argonne, IL 60439, USA*
- ⁹*University of Arizona, Tucson, AZ 85721, USA*
- ¹⁰*Universidad Nacional de Asunción, San Lorenzo, Paraguay*
- ¹¹*University of Athens, Zografou GR 157 84, Greece*
- ¹²*Universidad del Atlántico, Barranquilla, Atlántico, Colombia*
- ¹³*Augustana University, Sioux Falls, SD 57197, USA*
- ¹⁴*University of Bern, CH-3012 Bern, Switzerland*
- ¹⁵*Beykent University, Istanbul, Turkey*
- ¹⁶*University of Birmingham, Birmingham B15 2TT, United Kingdom*
- ¹⁷*Università di Bologna, 40127 Bologna, Italy*
- ¹⁸*Boston University, Boston, MA 02215, USA*
- ¹⁹*University of Bristol, Bristol BS8 1TL, United Kingdom*
- ²⁰*Brookhaven National Laboratory, Upton, NY 11973, USA*
- ²¹*University of Bucharest, Bucharest, Romania*
- ²²*University of California Berkeley, Berkeley, CA 94720, USA*
- ²³*University of California Davis, Davis, CA 95616, USA*
- ²⁴*University of California Irvine, Irvine, CA 92697, USA*
- ²⁵*University of California Los Angeles, Los Angeles, CA 90095, USA*
- ²⁶*University of California Riverside, Riverside CA 92521, USA*
- ²⁷*University of California Santa Barbara, Santa Barbara, CA 93106, USA*
- ²⁸*California Institute of Technology, Pasadena, CA 91125, USA*
- ²⁹*University of Cambridge, Cambridge CB3 0HE, United Kingdom*
- ³⁰*Universidade Estadual de Campinas, Campinas - SP, 13083-970, Brazil*
- ³¹*Università di Catania, 2 - 95131 Catania, Italy*
- ³²*Universidad Católica del Norte, Antofagasta, Chile*
- ³³*Centro Brasileiro de Pesquisas Físicas, Rio de Janeiro, RJ 22290-180, Brazil*
- ³⁴*IRFU, CEA, Université Paris-Saclay, F-91191 Gif-sur-Yvette, France*
- ³⁵*CERN, The European Organization for Nuclear Research, 1211 Meyrin, Switzerland*
- ³⁶*Institute of Particle and Nuclear Physics of the Faculty of Mathematics and Physics of the Charles University, 180 00 Prague 8, Czech Republic*
- ³⁷*University of Chicago, Chicago, IL 60637, USA*
- ³⁸*Chung-Ang University, Seoul 06974, South Korea*
- ³⁹*CIEMAT, Centro de Investigaciones Energéticas, Medioambientales y Tecnológicas, E-28040 Madrid, Spain*
- ⁴⁰*University of Cincinnati, Cincinnati, OH 45221, USA*
- ⁴¹*Centro de Investigación y de Estudios Avanzados del Instituto Politécnico Nacional (Cinvestav), Mexico City, Mexico*
- ⁴²*Universidad de Colima, Colima, Mexico*
- ⁴³*University of Colorado Boulder, Boulder, CO 80309, USA*
- ⁴⁴*Colorado State University, Fort Collins, CO 80523, USA*

- ⁴⁵ *Columbia University, New York, NY 10027, USA*
- ⁴⁶ *Comisión Nacional de Investigación y Desarrollo Aeroespacial, Lima, Peru*
- ⁴⁷ *Centro de Tecnologia da Informacao Renato Archer, Amarais - Campinas, SP - CEP 13069-901*
- ⁴⁸ *Central University of South Bihar, Gaya, 824236, India*
- ⁴⁹ *Institute of Physics, Czech Academy of Sciences, 182 00 Prague 8, Czech Republic*
- ⁵⁰ *Czech Technical University, 115 19 Prague 1, Czech Republic*
- ⁵¹ *Laboratoire d'Annecy de Physique des Particules, Université Savoie Mont Blanc, CNRS, LAPP-IN2P3, 74000 Annecy, France*
- ⁵² *Daresbury Laboratory, Cheshire WA4 4AD, United Kingdom*
- ⁵³ *Dordt University, Sioux Center, IA 51250, USA*
- ⁵⁴ *Drexel University, Philadelphia, PA 19104, USA*
- ⁵⁵ *Duke University, Durham, NC 27708, USA*
- ⁵⁶ *Durham University, Durham DH1 3LE, United Kingdom*
- ⁵⁷ *University of Edinburgh, Edinburgh EH8 9YL, United Kingdom*
- ⁵⁸ *Universidad EIA, Envigado, Antioquia, Colombia*
- ⁵⁹ *Eötvös Loránd University, 1053 Budapest, Hungary*
- ⁶⁰ *Erciyes University, Kayseri, Turkey*
- ⁶¹ *Faculdade de Ciências da Universidade de Lisboa - FCUL, 1749-016 Lisboa, Portugal*
- ⁶² *Universidade Federal de Alfenas, Poços de Caldas - MG, 37715-400, Brazil*
- ⁶³ *Universidade Federal de Goiás, Goiania, GO 74690-900, Brazil*
- ⁶⁴ *Universidade Federal do ABC, Santo André - SP, 09210-580, Brazil*
- ⁶⁵ *Universidade Federal do Rio de Janeiro, Rio de Janeiro - RJ, 21941-901, Brazil*
- ⁶⁶ *Fermi National Accelerator Laboratory, Batavia, IL 60510, USA*
- ⁶⁷ *University of Ferrara, Ferrara, Italy*
- ⁶⁸ *University of Florida, Gainesville, FL 32611-8440, USA*
- ⁶⁹ *Florida State University, Tallahassee, FL, 32306 USA*
- ⁷⁰ *Fluminense Federal University, 9 Icaraí Niterói - RJ, 24220-900, Brazil*
- ⁷¹ *Università degli Studi di Genova, Genova, Italy*
- ⁷² *Georgian Technical University, Tbilisi, Georgia*
- ⁷³ *University of Granada & CAFPE, 18002 Granada, Spain*
- ⁷⁴ *Gran Sasso Science Institute, L'Aquila, Italy*
- ⁷⁵ *Laboratori Nazionali del Gran Sasso, L'Aquila AQ, Italy*
- ⁷⁶ *University Grenoble Alpes, CNRS, Grenoble INP, LPSC-IN2P3, 38000 Grenoble, France*
- ⁷⁷ *Universidad de Guanajuato, Guanajuato, C.P. 37000, Mexico*
- ⁷⁸ *Harish-Chandra Research Institute, Jhansi, Allahabad 211 019, India*
- ⁷⁹ *University of Hawaii, Honolulu, HI 96822, USA*
- ⁸⁰ *Hong Kong University of Science and Technology, Kowloon, Hong Kong, China*
- ⁸¹ *University of Houston, Houston, TX 77204, USA*
- ⁸² *University of Hyderabad, Gachibowli, Hyderabad - 500 046, India*
- ⁸³ *Idaho State University, Pocatello, ID 83209, USA*
- ⁸⁴ *Instituto de Física Corpuscular, CSIC and Universitat de València, 46980 Paterna, Valencia, Spain*
- ⁸⁵ *Instituto Galego de Física de Altas Enerxías, University of Santiago de Compostela, Santiago de Compostela, 15782, Spain*
- ⁸⁶ *Indian Institute of Technology Kanpur, Uttar Pradesh 208016, India*

- ⁸⁷ *Illinois Institute of Technology, Chicago, IL 60616, USA*
- ⁸⁸ *Imperial College of Science, Technology and Medicine, London SW7 2BZ, United Kingdom*
- ⁸⁹ *Indian Institute of Technology Guwahati, Guwahati, 781 039, India*
- ⁹⁰ *Indian Institute of Technology Hyderabad, Hyderabad, 502285, India*
- ⁹¹ *Indiana University, Bloomington, IN 47405, USA*
- ⁹² *Istituto Nazionale di Fisica Nucleare Sezione di Bologna, 40127 Bologna BO, Italy*
- ⁹³ *Istituto Nazionale di Fisica Nucleare Sezione di Catania, I-95123 Catania, Italy*
- ⁹⁴ *Istituto Nazionale di Fisica Nucleare Sezione di Ferrara, I-44122 Ferrara, Italy*
- ⁹⁵ *Istituto Nazionale di Fisica Nucleare Laboratori Nazionali di Frascati, Frascati, Roma, Italy*
- ⁹⁶ *Istituto Nazionale di Fisica Nucleare Sezione di Genova, 16146 Genova GE, Italy*
- ⁹⁷ *Istituto Nazionale di Fisica Nucleare Sezione di Lecce, 73100 - Lecce, Italy*
- ⁹⁸ *Istituto Nazionale di Fisica Nucleare Sezione di Milano Bicocca, 3 - I-20126 Milano, Italy*
- ⁹⁹ *Istituto Nazionale di Fisica Nucleare Sezione di Milano, 20133 Milano, Italy*
- ¹⁰⁰ *Istituto Nazionale di Fisica Nucleare Sezione di Napoli, I-80126 Napoli, Italy*
- ¹⁰¹ *Istituto Nazionale di Fisica Nucleare Sezione di Padova, 35131 Padova, Italy*
- ¹⁰² *Istituto Nazionale di Fisica Nucleare Sezione di Pavia, I-27100 Pavia, Italy*
- ¹⁰³ *Istituto Nazionale di Fisica Nucleare Laboratori Nazionali di Pisa, Pisa PI, Italy*
- ¹⁰⁴ *Istituto Nazionale di Fisica Nucleare Sezione di Roma, 00185 Roma RM, Italy*
- ¹⁰⁵ *Istituto Nazionale di Fisica Nucleare Roma Tor Vergata, 00133 Roma RM, Italy*
- ¹⁰⁶ *Istituto Nazionale di Fisica Nucleare Laboratori Nazionali del Sud, 95123 Catania, Italy*
- ¹⁰⁷ *Universidad Nacional de Ingeniería, Lima 25, Perú*
- ¹⁰⁸ *University of Insubria, Via Ravasi, 2, 21100 Varese VA, Italy*
- ¹⁰⁹ *University of Iowa, Iowa City, IA 52242, USA*
- ¹¹⁰ *Iowa State University, Ames, Iowa 50011, USA*
- ¹¹¹ *Institut de Physique des 2 Infinis de Lyon, 69622 Villeurbanne, France*
- ¹¹² *Institute for Research in Fundamental Sciences, Tehran, Iran*
- ¹¹³ *Instituto Superior Técnico - IST, Universidade de Lisboa, 1049-001 Lisboa, Portugal*
- ¹¹⁴ *Instituto Tecnológico de Aeronáutica, Sao Jose dos Campos, Brazil*
- ¹¹⁵ *Iwate University, Morioka, Iwate 020-8551, Japan*
- ¹¹⁶ *Jackson State University, Jackson, MS 39217, USA*
- ¹¹⁷ *Jawaharlal Nehru University, New Delhi 110067, India*
- ¹¹⁸ *Jeonbuk National University, Jeonrabuk-do 54896, South Korea*
- ¹¹⁹ *Jyväskylä University, FI-40014 Jyväskylä, Finland*
- ¹²⁰ *Kansas State University, Manhattan, KS 66506, USA*
- ¹²¹ *Kavli Institute for the Physics and Mathematics of the Universe, Kashiwa, Chiba 277-8583, Japan*
- ¹²² *High Energy Accelerator Research Organization (KEK), Ibaraki, 305-0801, Japan*
- ¹²³ *Korea Institute of Science and Technology Information, Daejeon, 34141, South Korea*
- ¹²⁴ *National Institute of Technology, Kure College, Hiroshima, 737-8506, Japan*
- ¹²⁵ *Taras Shevchenko National University of Kyiv, 01601 Kyiv, Ukraine*
- ¹²⁶ *Lancaster University, Lancaster LA1 4YB, United Kingdom*
- ¹²⁷ *Lawrence Berkeley National Laboratory, Berkeley, CA 94720, USA*
- ¹²⁸ *Laboratório de Instrumentação e Física Experimental de Partículas, 1649-003 Lisboa and 3004-516 Coimbra, Portugal*
- ¹²⁹ *University of Liverpool, L69 7ZE, Liverpool, United Kingdom*

- ¹³⁰*Los Alamos National Laboratory, Los Alamos, NM 87545, USA*
- ¹³¹*Louisiana State University, Baton Rouge, LA 70803, USA*
- ¹³²*Laboratoire de Physique des Deux Infinis Bordeaux - IN2P3, F-33175 Gradignan, Bordeaux, France,*
- ¹³³*University of Lucknow, Uttar Pradesh 226007, India*
- ¹³⁴*Madrid Autonoma University and IFT UAM/CSIC, 28049 Madrid, Spain*
- ¹³⁵*Johannes Gutenberg-Universität Mainz, 55122 Mainz, Germany*
- ¹³⁶*University of Manchester, Manchester M13 9PL, United Kingdom*
- ¹³⁷*Massachusetts Institute of Technology, Cambridge, MA 02139, USA*
- ¹³⁸*University of Medellín, Medellín, 050026 Colombia*
- ¹³⁹*University of Michigan, Ann Arbor, MI 48109, USA*
- ¹⁴⁰*Michigan State University, East Lansing, MI 48824, USA*
- ¹⁴¹*Università di Milano Bicocca , 20126 Milano, Italy*
- ¹⁴²*Università degli Studi di Milano, I-20133 Milano, Italy*
- ¹⁴³*University of Minnesota Duluth, Duluth, MN 55812, USA*
- ¹⁴⁴*University of Minnesota Twin Cities, Minneapolis, MN 55455, USA*
- ¹⁴⁵*University of Mississippi, University, MS 38677 USA*
- ¹⁴⁶*Università degli Studi di Napoli Federico II , 80138 Napoli NA, Italy*
- ¹⁴⁷*Nikhef National Institute of Subatomic Physics, 1098 XG Amsterdam, Netherlands*
- ¹⁴⁸*National Institute of Science Education and Research (NISER), Odisha 752050, India*
- ¹⁴⁹*University of North Dakota, Grand Forks, ND 58202-8357, USA*
- ¹⁵⁰*Northern Illinois University, DeKalb, IL 60115, USA*
- ¹⁵¹*Northwestern University, Evanston, IL 60208, USA*
- ¹⁵²*University of Notre Dame, Notre Dame, IN 46556, USA*
- ¹⁵³*University of Novi Sad, 21102 Novi Sad, Serbia*
- ¹⁵⁴*Occidental College, Los Angeles, CA 90041*
- ¹⁵⁵*Ohio State University, Columbus, OH 43210, USA*
- ¹⁵⁶*Oregon State University, Corvallis, OR 97331, USA*
- ¹⁵⁷*University of Oxford, Oxford, OX1 3RH, United Kingdom*
- ¹⁵⁸*Pacific Northwest National Laboratory, Richland, WA 99352, USA*
- ¹⁵⁹*Università degli Studi di Padova, I-35131 Padova, Italy*
- ¹⁶⁰*Panjab University, Chandigarh, 160014, India*
- ¹⁶¹*Université Paris-Saclay, CNRS/IN2P3, IJCLab, 91405 Orsay, France*
- ¹⁶²*Université Paris Cité, CNRS, Astroparticule et Cosmologie, Paris, France*
- ¹⁶³*University of Parma, 43121 Parma PR, Italy*
- ¹⁶⁴*Università degli Studi di Pavia, 27100 Pavia PV, Italy*
- ¹⁶⁵*University of Pennsylvania, Philadelphia, PA 19104, USA*
- ¹⁶⁶*Pennsylvania State University, University Park, PA 16802, USA*
- ¹⁶⁷*Physical Research Laboratory, Ahmedabad 380 009, India*
- ¹⁶⁸*Università di Pisa, I-56127 Pisa, Italy*
- ¹⁶⁹*University of Pittsburgh, Pittsburgh, PA 15260, USA*
- ¹⁷⁰*Pontificia Universidad Católica del Perú, Lima, Perú*
- ¹⁷¹*University of Puerto Rico, Mayaguez 00681, Puerto Rico, USA*
- ¹⁷²*Punjab Agricultural University, Ludhiana 141004, India*
- ¹⁷³*Queen Mary University of London, London E1 4NS, United Kingdom*

- ¹⁷⁴*Radboud University, NL-6525 AJ Nijmegen, Netherlands*
- ¹⁷⁵*Rice University, Houston, TX 77005*
- ¹⁷⁶*University of Rochester, Rochester, NY 14627, USA*
- ¹⁷⁷*Royal Holloway College London, London, TW20 0EX, United Kingdom*
- ¹⁷⁸*Rutgers University, Piscataway, NJ, 08854, USA*
- ¹⁷⁹*STFC Rutherford Appleton Laboratory, Didcot OX11 0QX, United Kingdom*
- ¹⁸⁰*Università del Salento, 73100 Lecce, Italy*
- ¹⁸¹*Universidad del Magdalena, Santa Marta - Colombia*
- ¹⁸²*Sapienza University of Rome, 00185 Roma RM, Italy*
- ¹⁸³*Universidad Sergio Arboleda, 11022 Bogotá, Colombia*
- ¹⁸⁴*University of Sheffield, Sheffield S3 7RH, United Kingdom*
- ¹⁸⁵*SLAC National Accelerator Laboratory, Menlo Park, CA 94025, USA*
- ¹⁸⁶*University of South Carolina, Columbia, SC 29208, USA*
- ¹⁸⁷*South Dakota School of Mines and Technology, Rapid City, SD 57701, USA*
- ¹⁸⁸*South Dakota State University, Brookings, SD 57007, USA*
- ¹⁸⁹*Southern Methodist University, Dallas, TX 75275, USA*
- ¹⁹⁰*Stony Brook University, SUNY, Stony Brook, NY 11794, USA*
- ¹⁹¹*Sanford Underground Research Facility, Lead, SD, 57754, USA*
- ¹⁹²*University of Sussex, Brighton, BN1 9RH, United Kingdom*
- ¹⁹³*Syracuse University, Syracuse, NY 13244, USA*
- ¹⁹⁴*Universidade Tecnológica Federal do Paraná, Curitiba, Brazil*
- ¹⁹⁵*Tel Aviv University, Tel Aviv-Yafo, Israel*
- ¹⁹⁶*Texas A&M University, College Station, Texas 77840*
- ¹⁹⁷*Texas A&M University - Corpus Christi, Corpus Christi, TX 78412, USA*
- ¹⁹⁸*University of Texas at Arlington, Arlington, TX 76019, USA*
- ¹⁹⁹*University of Texas at Austin, Austin, TX 78712, USA*
- ²⁰⁰*University of Toronto, Toronto, Ontario M5S 1A1, Canada*
- ²⁰¹*Tufts University, Medford, MA 02155, USA*
- ²⁰²*Universidade Federal de São Paulo, 09913-030, São Paulo, Brazil*
- ²⁰³*Ulsan National Institute of Science and Technology, Ulsan 689-798, South Korea*
- ²⁰⁴*University College London, London, WC1E 6BT, United Kingdom*
- ²⁰⁵*Universidad Nacional Mayor de San Marcos, Lima, Peru*
- ²⁰⁶*Valley City State University, Valley City, ND 58072, USA*
- ²⁰⁷*University of Vigo, E- 36310 Vigo Spain*
- ²⁰⁸*Virginia Tech, Blacksburg, VA 24060, USA*
- ²⁰⁹*University of Warsaw, 02-093 Warsaw, Poland*
- ²¹⁰*University of Warwick, Coventry CV4 7AL, United Kingdom*
- ²¹¹*Wellesley College, Wellesley, MA 02481, USA*
- ²¹²*Wichita State University, Wichita, KS 67260, USA*
- ²¹³*William and Mary, Williamsburg, VA 23187, USA*
- ²¹⁴*University of Wisconsin Madison, Madison, WI 53706, USA*
- ²¹⁵*Yale University, New Haven, CT 06520, USA*
- ²¹⁶*Yerevan Institute for Theoretical Physics and Modeling, Yerevan 0036, Armenia*
- ²¹⁷*York University, Toronto M3J 1P3, Canada*

E-mail: sungbino@fnal.gov

ABSTRACT: This paper introduces a novel track-length extension fitting algorithm for measuring the kinetic energies of inelastically interacting particles in liquid argon time projection chambers (LArTPCs). The algorithm finds the most probable offset in track length for a track-like object by comparing the measured ionization density as a function of position with a theoretical prediction of the energy loss as a function of the energy, including models of electron recombination and detector response. The algorithm can be used to measure the energies of particles that interact before they stop, such as charged pions that are absorbed by argon nuclei. The algorithm's energy measurement resolutions and fractional biases are presented as functions of particle kinetic energy and number of track hits using samples of stopping secondary charged pions in data collected by the ProtoDUNE-SP detector, and also in a detailed simulation. Additional studies describe the impact of the dE/dx model on energy measurement performance. The method described in this paper to characterize the energy measurement performance can be repeated in any LArTPC experiment using stopping secondary charged pions.

KEYWORDS: Noble liquid detectors (scintillation, ionization, single-phase), Time projection chambers, Large detector systems for particle and astroparticle physics

Contents

1	Introduction	1
2	The track-length extension fitting algorithm	3
2.1	Gaussian approximation	5
2.2	Maximum-likelihood	6
3	The ProtoDUNE-SP detector	7
4	Beam instrumentation	10
5	Simulation and reconstruction	10
5.1	Simulation	10
5.2	Reconstruction of events in the TPC	10
6	Energy measurement performance	11
6.1	Stopping charged pions as a validation sample	11
6.2	Algorithm parameters	12
6.3	Performance in MC simulation sample using true E_K as the reference	14
6.4	Performance in data and MC simulation samples using E_K^{full} as the reference	18
6.5	Impact of dE/dx modeling	24
6.5.1	Reproduction of data dE/dx distributions	25
6.5.2	Modified box model parameter uncertainties	26
6.5.3	Impact on $\chi^2_{\pi^\pm}$	26
6.5.4	Results	28
7	Summary	32

1 Introduction

The observation of neutrino oscillations [1, 2] has opened a new window for the field of particle physics. The fact that neutrinos oscillate in flavor implies not only that some neutrino mass eigenstates have nonzero masses, but it also provides the possibility to contribute to our understanding of the broken baryon number asymmetry of the universe [3].

The liquid argon time projection chamber (LArTPC) [4] is a leading detector technology which has been proposed to answer the important questions described above [5]. In LArTPCs, the argon serves simultaneously as the target for neutrino interactions and as the sensitive detector material. Neutrinos interact primarily with argon nuclei, but they may also scatter off the electrons in the argon atoms. Particles produced by these interactions travel through the liquid argon, ionizing

argon atoms along their paths. In an applied electric field, some of the electrons liberated from the argon atoms will drift towards collection wires or pixels, while other electrons will recombine with the positively-charged argon ions. Scintillation light with a wavelength of 128 nm is produced abundantly along the paths of ionizing tracks in liquid argon. The liquid itself is transparent to this light. By collecting the drifting electrons and the scintillation photons, LArTPCs can record neutrino interactions with 10% level energy resolution [6], mm-scale position resolution based on collection wire or pixel spacing, and ns order timing resolution from photon detection systems.

Neutrino beams for experiments using LArTPCs typically have wide energy spectra over several GeV with average energies of the order of a GeV. Neutrino oscillation probabilities depend on L/E , where L is the distance from the production point to the detector, and E is the neutrino energy. The distance L is well known, but the energy E must be measured for each neutrino scattering event, both in the near detectors and the far detectors. The neutrino energy must be estimated from the observed secondary particles produced in the interaction of the neutrino and an argon atom. These particles consist of charged leptons, protons, charged pions, photons, neutrons, kaons, and other shorter-lived particles that decay into the particles listed. Because the beams have broad energy spectra, a number of different scattering process categories are possible: quasielastic scattering, resonant scattering and deep inelastic scattering [7].

The dense detection material in a LArTPC introduces a challenge by causing secondary interactions of hadrons originating from the neutrino scatter with other argon atoms in the detector. Because the lengths of the tracks of interacting particles are shorter than those of stopping particles with the same energies, range-based energy estimations are insufficient for interacting particles. Furthermore, interactions between hadrons and nuclei typically produce particles for which the energy is difficult or impossible to determine, such as neutrons and heavy nuclear fragments. Calorimetric energy measurements therefore only collect a fraction of the total energy of the incident particle, and that fraction varies from interaction to interaction in a random way which is difficult to model. Usually, calorimetric methods must be calibrated in situ with particles of known species and energies.

In this paper, we introduce a new method for energy measurement which can be utilized in a LArTPC. It is based on a fit for the best track-length extension using calorimetric and position information of hits on a reconstructed track. For an inelastically interacting particle, the method calculates the total track length the particle would have traveled if it had not interacted inelastically. Therefore, the method addresses the challenges introduced in the above paragraph. Data and simulation samples of the ProtoDUNE-SP detector [8, 9] are used to evaluate the performance. The method shows good performance for energy measurement on short tracks produced by interacting charged pions.

This paper is organized as follows. In Section 2, we introduce the track-length extension fitting (TLEFit) algorithm. Section 3 introduces the ProtoDUNE-SP detector and beam instrumentation, and Section 5 describes event reconstruction and the detector simulation. In Section 6, studies for the performance of the TLEFit algorithm are presented. Then, the paper concludes with a summary in Section 7.

2 The track-length extension fitting algorithm

Before introducing the track-length extension fitting (TLEFit) algorithm, it is important to discuss the basic operational principle of a LArTPC. A particle's activity inside liquid argon liberates electrons from argon atoms. A portion of these electrons recombines with argon ions, emitting photons. In general, a LArTPC experiment consists of a cathode plane and one or more anode planes to apply an electric field. The electrons drift toward the anode planes in this field, inducing electric signals in collection wires or pixels around the anode plane. Photon detection systems also collect the photons. The signals in the collection wires or pixels are recorded as functions of time within a time window. Since photons propagate much faster than drifting electrons, the trigger system that defines the starting point of the time window relies on photon detection systems.

For LArTPC experiments with collection wires, 2D space points are reconstructed by identifying peaks in the waveform of the electric signal. The combination of multiple collection wire planes with different orientations provides the capability to reconstruct 3D space points. In LArTPC experiments with readout pixels, a peak in the waveform represents a 3D space point. The deposited energy for a 3D space point is measured using the area around the peak in the waveform. Physical objects corresponding to traces of particles that traveled inside the LArTPC are produced by clustering the 3D space points with their positions and deposited energies (or hits hereafter). These physical objects are generally categorized as shower-like objects or track-like objects.

Particles such as muons, charged pions and protons ionize argon atoms in long, narrow trails. The drifted electrons are used to reconstruct track trajectories in the detector. The average energy loss per unit length (dE/dx) is well described by the Bethe–Bloch formula [10],

$$\left\langle \frac{dE}{dx} \right\rangle = \frac{\rho K Z}{A \beta^2} \left[\frac{1}{2} \ln \left(\frac{2m_e c^2 \beta^2 \gamma^2 W_{\max}}{I^2} \right) - \beta^2 - \frac{\delta}{2} \right], \quad (2.1)$$

where $m_e = 0.511 \text{ MeV}/c^2$ is the electron mass and $K = 0.307075 \text{ MeV cm}^2/\text{mol}$. The parameters $\beta = v/c$ and $\gamma = (1 - \beta^2)^{-1/2}$ are for the particle traveling inside the material. For liquid argon, the density $\rho = 1.39 \text{ g/cm}^3$, the atomic number $Z = 18$, the atomic mass $A = 39.948 \text{ g/mol}$, and the average excitation energy $I = 188.0 \times 10^{-6} \text{ MeV}$. The maximum transferable energy W_{\max} is defined as

$$W_{\max} = \frac{2m_e c^2 \beta^2 \gamma^2}{1 + \frac{2\gamma m_e}{M} + \frac{m_e^2}{M^2}}, \quad (2.2)$$

where M is the mass of the traveling particle. The last term of Eq 2.1 is the density correction,

$$\delta = \begin{cases} 2 \ln(\beta\gamma), & \text{if } \log_{10}(\beta\gamma) > y_1 \\ 0, & \text{if } \log_{10}(\beta\gamma) < y_0 \\ 2 \ln(\beta\gamma) - C + a[y_1 - \log_{10}(\beta\gamma)]^k, & \text{otherwise,} \end{cases} \quad (2.3)$$

where $y_0 = 0.2$, $y_1 = 3.0$, $C = 5.2146$, $a = 0.19559$, and $k = 3.0$. For kinetic energies above tens of MeV, which is the threshold for particles to be reconstructed as tracks, nuclear effects in energy deposition is negligible.

While the energy lost by an ionizing particle in a thin slice of material is distributed according to the Landau distribution [10], a particle traveling a long distance (more than a few cm) through

a material will experience an energy loss with an approximately Gaussian distribution due to the large number of ionization interactions and the central limit theorem. As a result, the continuous slowing down approximation (CSDA) based on Eq 2.1 for the average energy loss can be used to relate a particle’s initial energy to its range in the material [10]. If a particle only undergoes multiple scattering and ionization energy loss before it stops, its initial energy can be estimated from its range with percent-level accuracy [11].

If a particle interacts inelastically, however, the range cannot be used to estimate its energy. Its track is cut off due to the interaction, so the range would result in an energy estimate lower than the true value. Therefore, neutrino experiments with LArTPCs have been using the visible energy [12, 13], which is defined to be the sum of energy deposits left by the track object and all of its daughters (and their daughters) created in interactions with the liquid argon. Unfortunately, it works well only when all daughters have enough energy to be reconstructed and the contribution from undetected neutrons is small.

The TLEFit algorithm introduced in this paper is a new energy measurement method which overcomes the weaknesses of the range-based estimation and visible energy-based estimation. Figure 1 shows an example with hits of a reconstructed charged pion track. The abscissa is the residual range, which is defined for a hit on a charged particle’s trajectory as the length from the trajectory’s end point to the hit, following along the trajectory. The ordinate is dE/dx in MeV/cm units. The average dE/dx distribution of charged pions as a function of residual range is shown with the red solid line based on the Bethe-Bloch formula in liquid argon (LAr). A dE/dx distribution of an inelastically interacting charged pion is shown with a prefit dE/dx label. The measured dE/dx values are obtained from the measured ionization charge density corrected for electron drift lifetime and recombination effects, as well as the charge yield expected per MeV of energy loss in LAr. There is a gap between the prefit dE/dx distribution and the vertical axis because first and last several hits are not included in the fit. They could be hits with incomplete dE/dx or only noise. This is discussed in more detail in Section 6.2. To measure the energy of a charged pion that has interacted inelastically with the argon, we look for an offset in the residual range which makes the residual range and dE/dx distribution agree best with the known physics for passage of charged particle through liquid argon. That offset is added to the original track length to estimate the best track-length. This is the track length that the particle with the prefit dE/dx distribution would have traveled until it stopped if it did not interact inelastically. Finally, energy at the starting point of the track is measured using the CSDA and the best track-length. The post fit dE/dx distribution with the best offset is also shown.

Based on the residual range vs. dE/dx curve derived from the Bethe-Bloch formula, shown in figure 1, it could be easily expected that energy measurement performance will highly depend on particle’s initial kinetic energy (E_K). Short residual range region that corresponds to low E_K of charged pions exhibits stiff slopes, commonly referred to as the Bragg peak region. Since dE/dx varies rapidly as a function of residual range, it is easier to find the best offset in this region compared to longer residual range region, known as the MIP (minimum-ionizing particle) region, that has much smaller slopes. For an inelastically interacting charged pion track for which all hits have MIP-like energy deposit around 2 MeV/cm, the TLEFit algorithm cannot work well. This is shown in Section 6.

One of the most important parts of the TLEFit is the procedure to calculate the best offset.

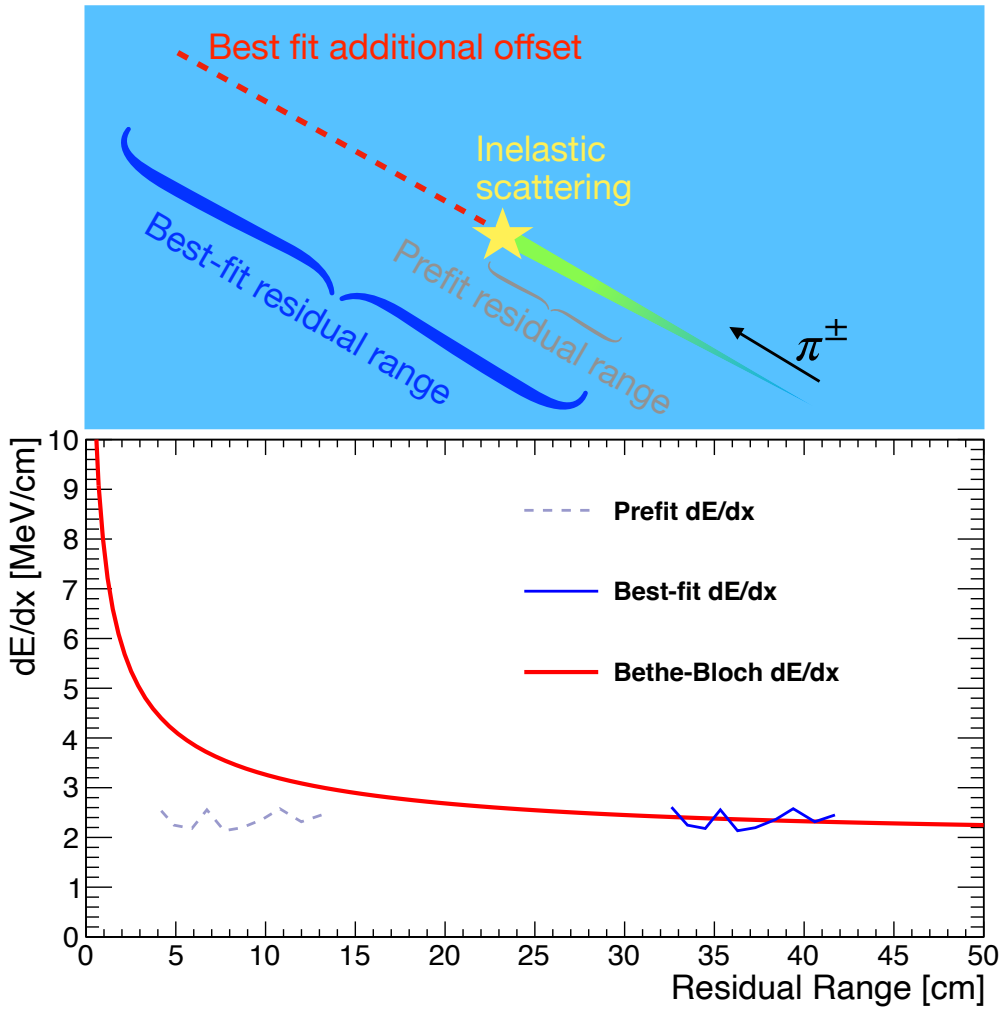


Figure 1: This figure illustrates the TLEFit method. In the bottom figure, the red solid line shows the mean energy loss $\langle dE/dx \rangle$ as a function of distance from the stopping point (residual range) using Eq. 2.1 for a charged pion in LAr. An example of measured dE/dx for an interacting charged pion is shown with a dashed line. The solid blue line shows the same measured dE/dx curve with an additional offset on range with best match with the red solid line.

This paper describes and compares two methods. One method is based on minimizing a χ^2 function assuming Gaussian distributions of inputs, and the second method is based on maximizing a likelihood function.

2.1 Gaussian approximation

The simplest way to score the agreement between the Bethe–Bloch curve and the measured dE/dx distribution is by calculating the χ^2 between them. Many LArTPC experiments have employed χ^2 -based particle identification scores [14]. Therefore, we describe this method before introducing a likelihood-based method.

For a given position offset L' , we define

$$\chi^2(L') = \sum_{i=1}^{N_{\text{hits}}} \left[\frac{dE}{dx}(\text{Measured}; i) - \frac{dE}{dx}(\text{Bethe-Bloch}; \text{range}_i + L') \right]^2. \quad (2.4)$$

The dE/dx term noted with the Bethe-Bloch on the right-hand side in Eq. 2.4 is the expected dE/dx from the CSDA using the track length given by the sum of hit's residual range and an additional offset, L' . By looking for the offset which gives the minimum χ^2 value, the energy of the interacted particle can be measured. We should note that Eq. 2.4 is based on an assumption that measured dE/dx follows Gaussian distributions with mean values given by the Bethe-Bloch formula in Eq. 2.1.

2.2 Maximum-likelihood

The measured dE/dx does not always follow a Gaussian distribution. This approximation is valid when there are sufficient interactions so that outlying energy loss such as high-energy δ -ray emission contribute a small fraction of the total energy loss.

It is well known that the probability density function (PDF) of dE/dx for ionizing particle is described by the Vavilov function [15]. In this paper, the significance parameter, κ , is used to define regions for the Vavilov function and its approximated versions, the Landau and the Gaussian functions. The parameter κ is defined as

$$\kappa = \frac{\xi}{W_{\text{max}}}, \quad (2.5)$$

where

$$\xi = \frac{\rho K Z}{2A\beta^2} \delta x, \quad (2.6)$$

with δx denoting the distance that the particle traveled in cm. The other variables are defined in the same way as in Eq. 2.1. The κ ranges that define PDFs for dE/dx are selected as

$$\text{PDF for } dE/dx : \begin{cases} \text{Gaussian} & , \text{ if } \kappa > 10 \\ \text{Vavilov} & , \text{ if } 0.01 < \kappa < 10 \\ \text{Landau} & , \text{ if } \kappa < 0.01 \end{cases} \quad (2.7)$$

following the Section PHYS332 of Geant [16]. The κ distribution as a function of E_K is shown in figure 2 for charged pion and proton in LAr. Note that κ is a function of δx and the typical pitch of hits in ProtoDUNE-SP, 0.65 cm, is used in the figure.

The PDFs with several E_K values for charged pions and protons are shown in figure 3. Mean dE/dx value from the Bethe-Bloch formula and the most probable values (MPVs) of dE/dx from the Landau-Vavilov-Bichsel formula [17] are presented together in dashed green lines and dashed blue lines, respectively. We can see that the Gaussian approximation introduced in Section 2.1 is not a good choice for particles with κ much smaller than unity. In this case, the Bethe-Bloch formula cannot describe the peak of the PDF, and the shape of the PDF is also significantly different from the Gaussian. On the other hand, with κ values bigger than unity, the Bethe-Bloch formula shows good agreement with the peak position, and the PDF shapes become similar with the Gaussian.

Using the PDFs $P\left(\frac{dE}{dx} | E_K\right)$ where P stands for the probability, a joint likelihood (\mathcal{L}) is calculated by multiplying the dE/dx probabilities for each hit. For the TLEFit, the expected E_K of

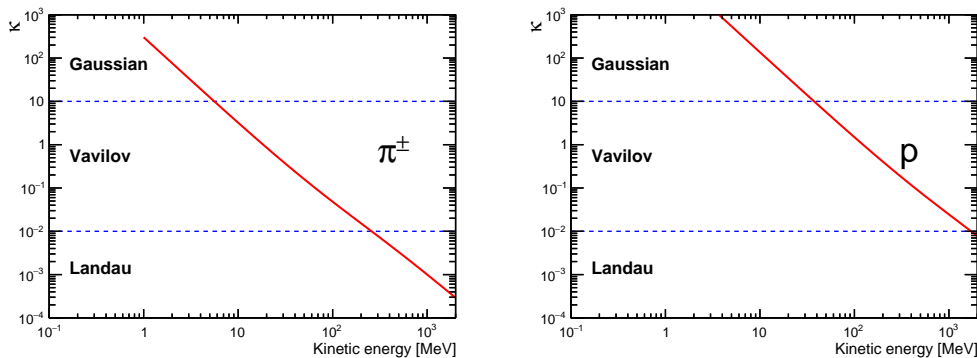


Figure 2: Three regions are defined using the κ value. If $\kappa > 10$, the Gaussian PDF is used. If $\kappa < 0.01$, the Landau PDF is used. Otherwise, the Vavilov PDF is used. Plots are drawn for charged pions (left) and protons (right) in LAr using typical pitch (0.65 cm) of the ProtoDUNE-SP.

particle at a hit is calculated using the CSDA and the length given by sum of hit's residual range and an additional offset. As a result, the total likelihood for a given offset, L' , is written as

$$-2 \ln \mathcal{L}(L') = -2 \sum_{i=1}^{N_{\text{hits}}} \ln P \left(\frac{dE}{dx} (\text{Measured}; i) \left| E_K^{\text{CSDA}}(\text{range}_i + L') \right. \right). \quad (2.8)$$

By looking for the best offset which gives the minimum $-2 \ln \mathcal{L}$ value, energy of the interacted particle can be estimated through CSDA.

3 The ProtoDUNE-SP detector

The ProtoDUNE single-phase (ProtoDUNE-SP) apparatus at CERN [8, 18] is designed as a test bed and full-scale prototype for the elements of the first far detector module of the Deep Underground Neutrino Experiment (DUNE) [19]. It is a single-phase LArTPC with an active volume of $7.2 \times 6.1 \times 7.0 \text{ m}^3$. The coordinate system is right-handed. The x axis is horizontal and is parallel with the nominal electric field directions and is perpendicular to the wire planes. The y axis is vertical (positive pointing up), and the z axis is horizontal and points approximately along the beam direction. A simplified schematic of the detector is shown in figure 4.

The time projection chamber (TPC) is divided into two parts by the cathode plane at the center ($x = 0 \text{ cm}$). The anode planes are placed at two sides opposite to the cathode plane. The nominal electric field strength is 500 V/cm. The maximum drift length in ProtoDUNE-SP is 3572 mm. This results in a maximum drift time of 2.25 ms.

The ProtoDUNE-SP TPC was built to test the segmented design of the DUNE horizontal drift far detector module, with full-size components. As a result, ProtoDUNE-SP contains six anode plane assemblies (APAs) arranged into the two anode planes, each consisting of three side-by-side APAs. The single cathode plane is composed of 18 cathode plane assembly (CPA) modules. The photon detector system comprises 60 optical modules, ten of which are installed in each APA. It is used to collect scintillation light produced by passing particles and test different photon collection technologies proposed for the DUNE far detector modules.

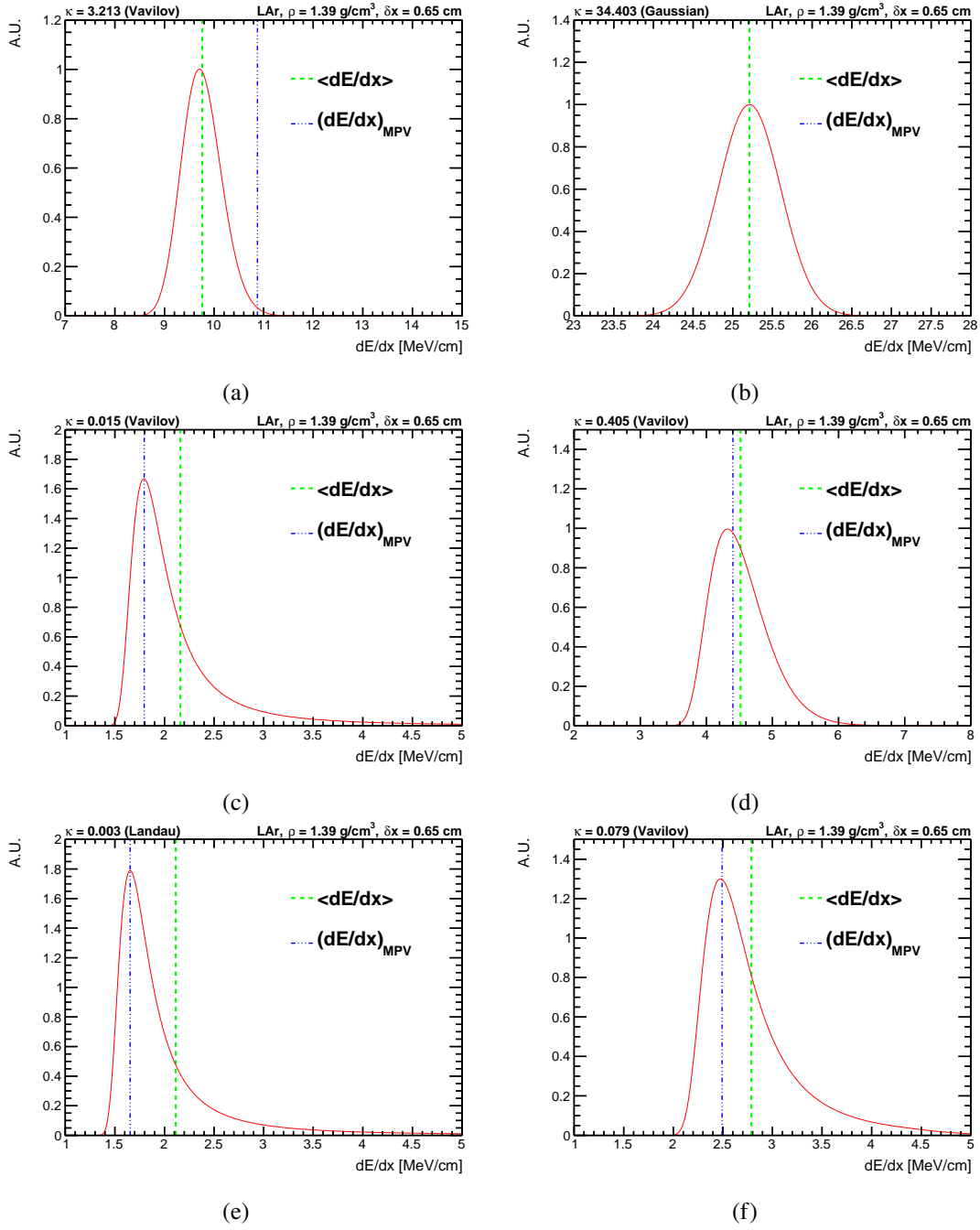


Figure 3: The dE/dx PDFs for charged pions (left) and protons (right) in LAr. For charged pions, PDFs are shown with E_K of 10 MeV (top), 200 MeV (center), and 500 MeV (bottom). For protons, PDFs are shown with E_K of 20 MeV (top), 200 MeV (center), and 500 MeV (bottom). Green lines show mean dE/dx values from Eq. 2.1 and blue lines show the most probable values (MPV) from the Landau-Vavilov-Bichsel formula. The κ values and used functions for PDFs are noted on top-left corners of plots.

Each APA has four wire planes. For reconstruction of particle tracks and showers, three planes (U , V and X) are used. The X plane has wires in parallel to the y axis with 4.79 mm pitch. The U and V planes have wires with 4.67 mm pitch which are oriented $\pm 35.7^\circ$ with respect to the y axis. The fourth plane is an uninstrumented grid plane on the drift side of the U plane. The spacing between the planes is 4.75 mm.

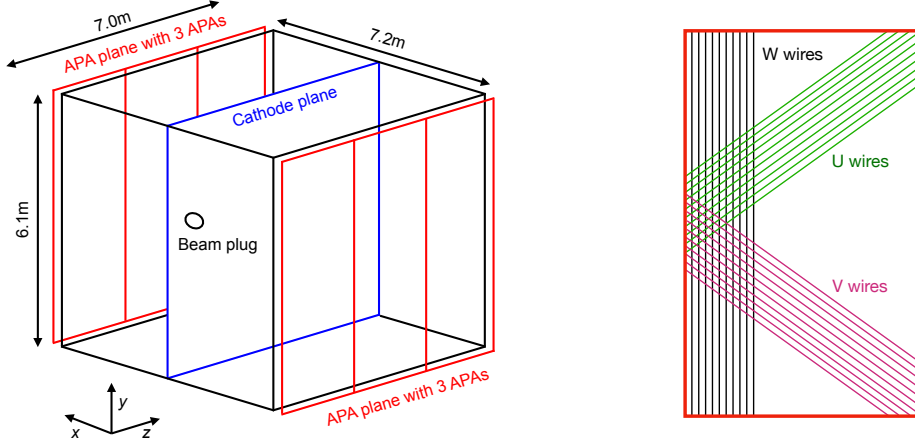


Figure 4: A simple drawing of the ProtoDUNE-SP detector (left) and an illustration of the three wire planes on an APA (right) are shown. A black box in the left figure represents the active volume, divided into two parts by the cathode at the center. The six APAs are arranged into two anode planes, each consisting of three side-by-side APAs. The test beam enters through the beam plug, close to the right side of the cathode. The right-handed coordinate system is shown in addition to the dimensions of the active volume. For wire planes, only ten wires for each plane are shown for clarity.

The construction and installation of the detector was finished in early July 2018. After commissioning, it started its operation from September 2018. For two months, October and November 2018, the ProtoDUNE-SP TPC was exposed to a tagged and momentum-analyzed particle beam with momentum settings ranging from 0.3 GeV/ c to 7 GeV/ c [20, 21] and collected more than four million events with incident beam particle inside the TPC. The standard deviation of the beam momentum distribution was measured to be approximately 7% by fitting Gaussian distributions to beam spectrometer data. The test beam entered the detector at mid-height and about 30 cm away from the cathode plane, on the negative x side with angles 11° down from the horizontal and 10° to the right of the z direction. At this angle, the spacing between three-dimensional reconstructed hits is approximately 0.65 cm. A beam plug was installed on the low- z , negative- x side of the TPC to minimize beam energy loss due to upstream materials. The cosmic ray tagger (CRT) with 6.8 m \times 6.8 m scintillation panels at both upstream and downstream of the ProtoDUNE-SP cryostat is used to tag cosmic and beam-halo muons. The detector continued to operate through July 2020, collecting data to test and validate the technologies for the future DUNE far detector modules, demonstrate operational stability, and explore operational parameters.

Additional information for design, construction, and operation of ProtoDUNE-SP can be found in [8]. First results for the detector calibration and response are published in [9].

4 Beam instrumentation

The upstream beam spectrometer measures the momenta of incident particles using a magnetic field and three planes of scintillating fibers. To remove ambiguity coming from multiple hits in a single plane, there should be exactly one particle reconstructed in the beam spectrometer for an event. The data sample collected with a nominal beam momentum of 1 GeV/ c is used in this study. To veto events with activities inside the TPC coming from beam halo, it is further required that both upstream and downstream CRTs should not have hits.

The beam instrumentation provides good particle identification performance between μ^+/π^+ and protons for 1 GeV/ c mode using the time-of-flight (Δt_F) information as described in [21]. In this paper, $\Delta t_F < 110$ ns requirement is used to study secondary charged pions coming from interactions between beam charged pions and argon atoms.

5 Simulation and reconstruction

In this paper, data events with incident beam particles inside ProtoDUNE-SP are used to study the performance of the TLEFit method.

5.1 Simulation

To generate Monte-Carlo (MC) simulated samples, the incident beam is modeled using the Geant4 [22] based package, G4beamline [23]. Detailed information for the beam line and its simulation is given in [20, 21].

Cosmic rays are simulated using CORSIKA v7.4 [24]. To completely cover the 3 ms detector readout window, cosmic rays are generated over a 6 ms time range with the center on the trigger time.

For the TPC simulation, Geant4 v4.10.3 with the QGSP_BERT physics list [22] is used to describe particle propagation and interactions. The detector response is modeled with LArSoft [25] using the WireCell toolkit [26].

5.2 Reconstruction of events in the TPC

The data processing procedure which reconstructs physical objects using waveforms from the anode wire planes is performed as described in [9]. It is summarized briefly below.

For each collection wire, the TPC readout electronics produces a digitized waveform using analog-to-digital converters (ADCs) that sample the current at 2 MHz. After noise removal, each waveform is deconvolved to reproduce the ionization charge distribution as a function of the drift time. Then, the hit finding algorithm fits the peaks in the deconvolved wire waveforms with Gaussian shapes. A hit represents a charge deposition on a single wire at a given time.

To reconstruct interactions inside the TPC, pattern recognition is performed with the Pandora software package [27]. The first step starts with two-dimensional clustering of hits in each detector readout plane. For 3D reconstruction, the 2D clusters are matched between different layers using

timing and shape information. The angles between the wires in the readout planes provide the necessary information to solve for the third coordinate. If there is ambiguity, the original two-dimensional clustering is changed using information from all three views until consistent matches between two-dimensional clusters is made. Finally, 3D hits are constructed and particle interaction hierarchies are created.

The Pandora software package also executes various algorithms to reconstruct an overall picture in the ProtoDUNE-SP TPC. First, all clusters are analyzed by an cosmic-ray hypothesis algorithm to identify and to remove clear cosmic-ray candidates. After removing energy deposits coming from these clear cosmic-ray candidates, a 3D slicing algorithm divides the detector into spatial regions with two hypotheses, cosmic ray and test beam, where a slice contains all of the hits from a single parent particle interaction. Then, a boosted decision tree (BDT) algorithm selects slices that contain clusters that originate from the test beam.

6 Energy measurement performance

The performance of the TLEFit method is tested using data and MC simulation samples of the ProtoDUNE-SP experiment. For this purpose, stopping charged pions are selected from the secondary particles resulting from the interaction between the charged pion beam and argon atoms. So, we introduce the selection for stopping charged pions first. It is validated that the CSDA can describe well the true E_K for selected stopping charged pion candidates. As a result, E_K from the CSDA is used as reference to compare performance of the TLEFit method between data and MC simulation samples. Tunable parameters of the TLEFit algorithm are also introduced. Then, E_K measurement performance of the TLEFit algorithm is presented. The fitting is performed using subsets of stopping charged pions' hits to mimic inelastically interacting charged pions. Therefore, algorithm performance is presented as functions of E_K and number of hits that are used for the fitting. For the MC simulation sample, the energy measurement performance is also presented using true E_K as reference with the same selection that is used for comparison between data and MC simulation samples. Finally, a systematic study related with impact of dE/dx modeling is performed to understand energy measurement scale difference between data and MC simulation samples.

6.1 Stopping charged pions as a validation sample

To characterize the energy measurement performance, a reference value of the true energy is required. For MC samples, the true energies are known for each particle at each step along their trajectories. But for data, there is no such perfect reference. Fortunately, the CSDA can provide a good reference for the E_K values of stopping charged pions. It is therefore important to filter out inelastically interacting charged pions from reconstructed charged pion candidates.

In this study, the discrimination is provided by $\chi_{\pi^\pm}^2$, which is defined to be

$$\chi_{\pi^\pm}^2 = \frac{1}{N_{\text{Hits}}^{\text{range}<26\text{cm}}} \sum_{i=0}^{\text{range}_i < 26\text{cm}} \left(\frac{dE}{dx}(\text{Measured}; i) - \frac{dE}{dx}(\text{Bethe-Bloch}, \pi^\pm; \text{range}_i) \right)^2 / \sigma^2. \quad (6.1)$$

Here, $\frac{dE}{dx}(\text{Bethe-Bloch}; \text{range}_i)$ is the expected dE/dx for a given residual range coming from the CSDA using the Bethe-Bloch formula in Eq. 2.1, and σ contains uncertainties of $\frac{dE}{dx}$ for both from

the CSDA and the TPC's energy measurement resolution. Since Eq. 6.1 uses hits with residual range less than 26 cm to make the $\chi^2_{\pi^\pm}$ not to be dominated by MIP hits, stopping charge pions with visible Bragg peaks have smaller χ^2 values compared to inelastically interacting charged pions. To produce a normalized χ^2 , number of hits included into the $\chi^2_{\pi^\pm}$, $N_{\text{Hits}}^{\text{range} < 26\text{cm}}$, is divided. Figure 5 shows the $\chi^2_{\pi^\pm}$ distribution as a function of true E_K in a MC sample of charged pions. A peak with $\chi^2_{\pi^\pm}$ value about from 2 to 4 is coming from stopping charged pions. The other peak that has $\chi^2_{\pi^\pm}$ value around 12 to 16 is coming from inelastically interacting charged pions that left tracks with length almost 26 cm or longer where all hits are MIP-like. That is the reason why the $\chi^2_{\pi^\pm}$ distribution of the band is approximately constant as a function of true E_K in the two dimensional distribution. Very high $\chi^2_{\pi^\pm}$ values greater than 20 are coming from inelastically interacted charged pions that left short tracks. In this study, $\chi^2_{\pi^\pm}$ value for the secondary charged pions is required to be smaller than 6.0 to select the stopping charged pions. Figure 6 shows that the CSDA with the full track length (E_K^{full}) estimates the true E_K (E_K^{true}) well after applying the $\chi^2_{\pi^\pm} < 6$ cut.

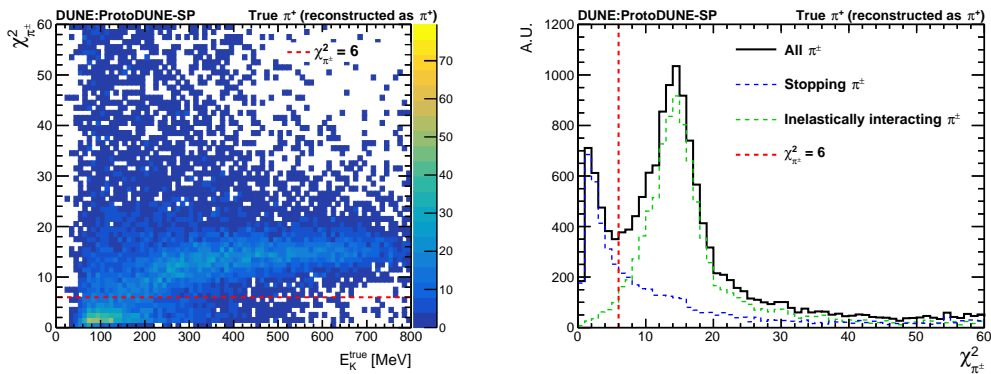


Figure 5: The $\chi^2_{\pi^\pm}$ distributions of charged pions in a MC sample are shown. Left plot shows a two dimensional distribution as a function of truth E_K . Right plot shows one dimensional distribution of $\chi^2_{\pi^\pm}$. Reconstructed charged pions which are matched with truth-level charged pions are used in this plot.

6.2 Algorithm parameters

Before the algorithm introduced in Sec. 2 can be applied to real data, several issues which affect the energy measurement performance must be addressed. We describe parameters of the algorithm that can be tuned in order to optimize the performance.

The first parameter is the minimum number of usable hits to include in the fit. In the case where two dE/dx PDFs overlap significantly between two different values of E_K , including only a small number of hits in the fit can lead to a huge uncertainty in the energy measurement. For example, the dE/dx PDFs of charged pions with 200 MeV and 500 MeV of E_K values have a large overlap as shown in figure 3. Therefore, fitting a small number of hits which have random dE/dx values given by PDFs will perform poorly. On the other hand, requiring many hits excludes low-energy particles, since E_K is highly correlated with the total length of the particle's trajectory. In this paper, at least 15 hits are required. This number corresponds to approximately 40 MeV of

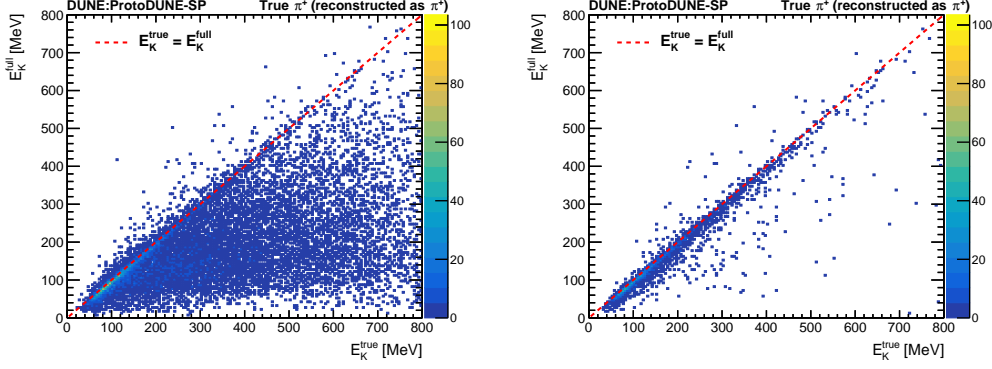


Figure 6: Plots show the relationship between truth-level and range-based kinetic energies for charged pions before (left) and after (right) applying the $\chi^2_{\pi^\pm} < 6$ cut, respectively. The same charged pion selection used in figure 5 is used.

kinetic energy threshold for charged pions inside the ProtoDUNE-SP TPC. This requirement can be optimized depending on the targeted E_K range of the particles under study.

The second parameter is related to poor dE/dx measurements in the first and last several hits of a track. These hits are affected by proximity to other ionizing particle activity, electric field distortions in the detector near the field cage, and the fact that the starting and the stopping points within the argon volume viewed by the last hit wire is unknown. The fact that charges are induced on nearby sense wires means that hits close to the track ends suffer from end effects, not just the last hit. In this paper, the first three hits and the last three hits are not included in the fitting. These are also tunable parameters of the algorithm. In addition, for a hit, dE/dx value measured by the collection plane is used.

The third parameter comes from the nature of the energy loss of particles. Figure 2 shows that dE/dx follows the Vavilov distribution where particles have E_K of hundreds of MeV. Therefore, hits with measured dE/dx values in either the low tail or the high tail of the Vavilov distribution are assigned low probabilities. This can cause the fit to converge to a poor result. To improve the reliability of the fit, hits with extreme measured values of dE/dx are truncated. In this paper, only hits with dE/dx of $0.5 \text{ MeV/cm} - 5 \text{ MeV/cm}$ are used for charged pions.

The last parameters are the adjustable step size (L_{step}) and the maximum additional track length (L_{max}). The value of L_{max} determines the maximum measurable E_K for a given track. The E_K given by CSDA using the original track length plus L_{max} becomes the maximum measurable E_K for that track. The L_{step} can affect the energy measurement resolution. Approximately $2.1 \text{ MeV/cm} \times L_{\text{step}}$ is the E_K step of the fitting in the E_K region up to several hundred MeV for charged pions. A longer L_{max} and a shorter L_{step} could improve the performance of the fits. But it also leads to fits that require more CPU time because fits evaluate Eq. 2.4 and Eq. 2.8 multiple times, namely L_{max} divided by L_{step} , to look for the best additional track length. In addition, having shorter L_{step} does not always provide better energy resolution. If the fitting itself has poorer energy resolution compared with $2.1 \text{ MeV/cm} \times L_{\text{step}}$, a smaller L_{step} does not improve the resolution and instead only takes more CPU time. In this paper, $L_{\text{max}} = 450 \text{ cm}$ is used, since the $1 \text{ GeV}/c$ primary

beam charged pion has about 870 MeV of E_K where the CSDA gives about 1000 MeV of E_K for charged pions with 450 cm of track length. For L_{step} , 1 cm is used targeting about 2 MeV of E_K measurement resolution.

The tunable parameters described above are summarized in Table 1.

Table 1: Summary of tunable parameters of the TLEFit algorithm.

Parameters	Used values	Impacts
Minimum number of hits	15	E_K acceptance & resolution
Skip first and last hits	3	Fitting performance
Truncate outlying dE/dx	Use 0.5 MeV/cm – 5 MeV/cm for π^\pm	Fitting performance
Maximum additional length	450 cm for π^\pm	Maximum measurable E_K & CPU time
Fitting step size	1.0 cm for π^\pm	E_K resolution & CPU time

6.3 Performance in MC simulation sample using true E_K as the reference

In this section, the energy measurement performance is presented in terms of resolution and fractional bias as functions of true E_K and the number of hits.

For example, if we have 50 hits for a charged pion, multiple fits are performed after vetoing several hits from the end of the track for fitting, using 49 hits, 48 hits, and so on. Then, resolution is measured for each fit. Resolution histograms are drawn as a function of E_K^{true} and number of hits, and their peaks are fit with a Gaussian function to extract the resolution and the fractional bias.

The CSDA using an incomplete track (E_K^{range}) underestimates the charged pion’s energy as shown in figure 7. The TLEFit algorithm can provide better energy measurement (E_K^{TLE}) by introducing the best additional track length. Figure 8 shows two-dimensional distributions of the fractional energy residual from the Gaussian approximation and the maximum-likelihood methods. The Gaussian approximation shows clear bands corresponding to biased energy measurements. These measurements occur when the best additional track length is found to be in the minimum ionizing E_K . The maximum-likelihood method plots show populations with biased energy measurements, but these are not concentrated into a band, as seen in the Gaussian approximation plots.

Equation 2.4 tends to have a minimum χ^2 value where $\frac{dE}{dx}$ (Bethe–Bloch; $\text{range}_i + L'$) is near its minimum point regardless of the true charged pion E_K . The band corresponds to the constant fitted pion energy that gives the minimum dE/dx in the Bethe–Bloch formula. This tendency becomes stronger with more hits in the MIP region. In the other words, this bias becomes more frequent with higher charged pion kinetic energies and with shorter reconstructed track lengths (smaller numbers of hits), which is well shown in figure 8.

This bias implies that the maximum-likelihood method is the most appropriate one for charged pions. Therefore, we fix the fitting method to maximum-likelihood. Figure 9 shows examples of histograms which are used to measure resolutions and fractional biases. The energy measurement resolution and fractional bias for each distribution are calculated using data points within $\pm 2\sigma$ of the fitted Gaussian function.

Figure 10 summarizes the extracted resolutions and fractional biases. The resolutions are better than 6.5%, and the fractional biases are smaller than 4%. Better resolutions are observed at lower E_K and with a greater number of hits. Lower E_K benefits from the steeper slope of dE/dx as a function of E_K , while a greater number of hits provides stronger constraints. Sizes of fractional biases are smaller than 1.5%, except for charged pions with 15 to 30 hits, which exhibit biases down to -3.5% at lower E_K .

From a study using MC truth information, we find that tracks with fewer hits tend to have shorter reconstructed total track lengths compared to the true track lengths. For a given E_K , a smaller number of hits implies that the track's angle relative to the anode plane is steeper, reducing the number of sense wires that can collect signals from the track. In such cases, the 3D spatial points of hits are reconstructed with larger uncertainties. Consequently, the residual ranges and their sum, the reconstructed total track length, are biased to be shorter than the true values. This effect is most pronounced in the smallest-hit region. However, the magnitude of the fractional bias, up to 3.5%, remains relatively small compared to the biases observed when using CSDA for inelastically interacting charged pions, as shown in Figure 7.

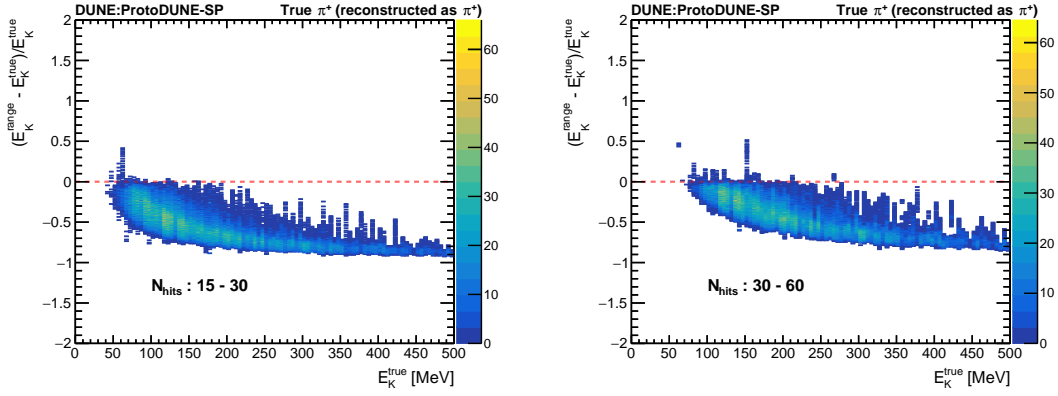


Figure 7: Two-dimensional distributions of the fractional energy residual from the CSDA with incomplete tracks, using 15 to 30 (left) and 30 to 60 (right) hits.

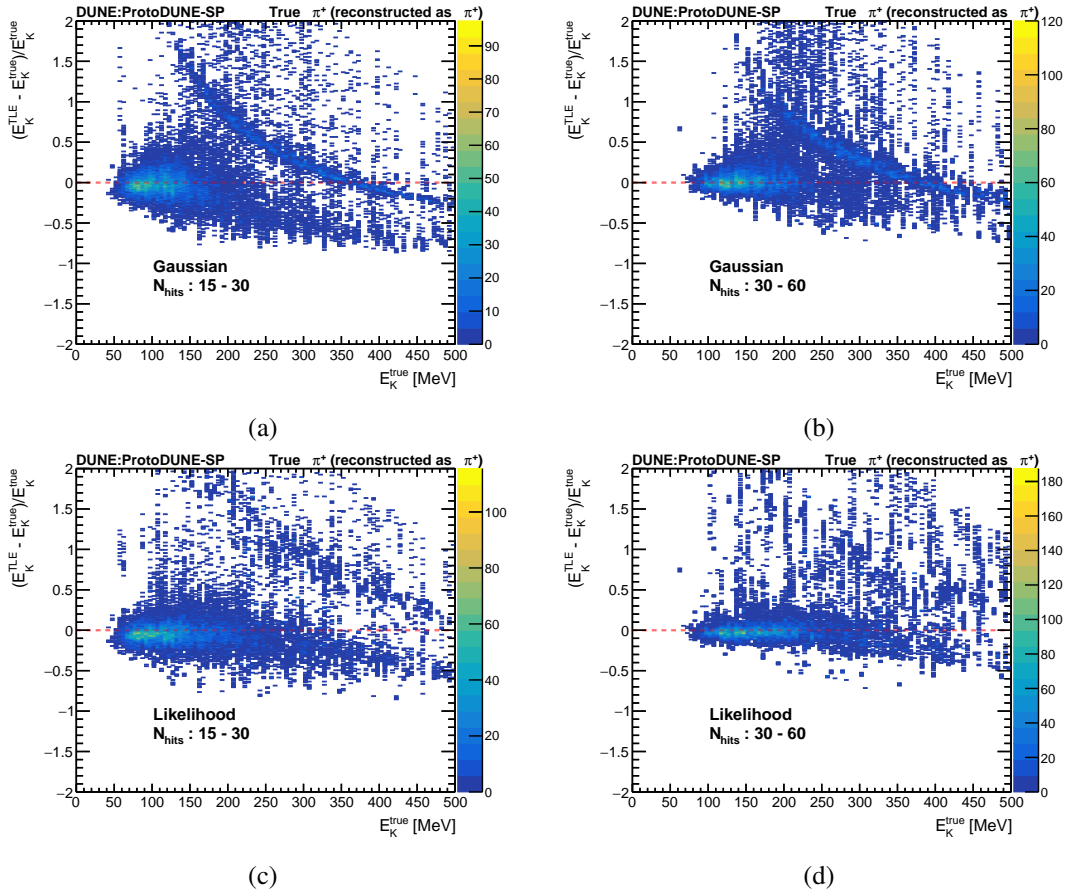


Figure 8: Example two-dimensional distributions of the fractional energy residual from the Gaussian approximation method (top) and the maximum-likelihood method (bottom), using 15 to 30 (left) and 30 to 60 (right) hits.

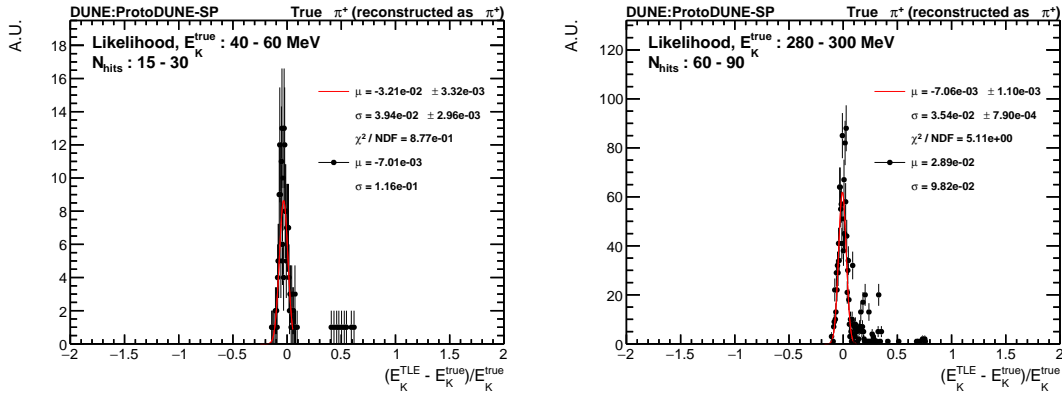


Figure 9: Example plots of energy measurement resolutions based on truth-level E_K . Distributions and Gaussian fit results with truth-level E_K from 40 to 60 MeV and 280 to 300 MeV with number of hits from 15 to 30 and 60 to 90 are shown in the top and bottom panels, respectively.

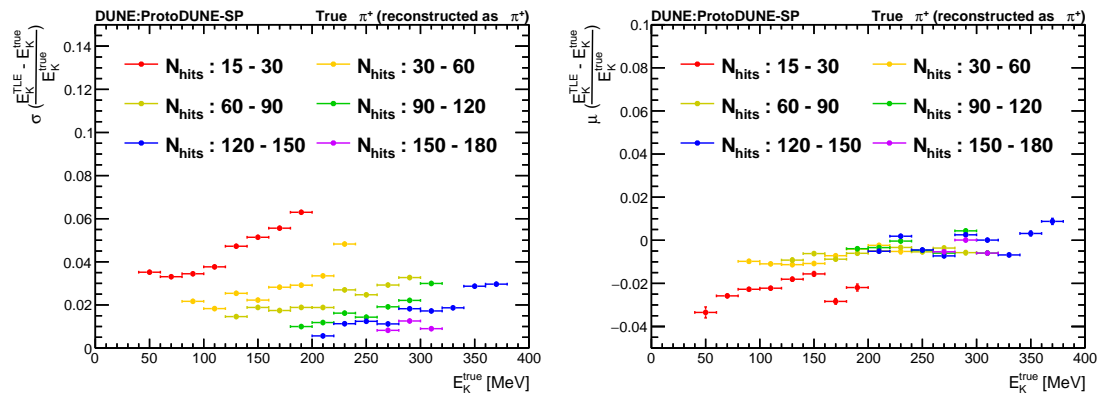


Figure 10: Summarized plots of energy measurement performance of the TLEFit method based on maximum-likelihood method using a MC sample. Resolutions (left) and fractional biases (right) are shown as functions of charged pions' true E_K and number of hits.

6.4 Performance in data and MC simulation samples using E_K^{full} as the reference

The same study is performed using the E_K from the CSDA with E_K^{full} as the reference instead of the true energy to investigate performance for real data and to directly compare results from MC simulation and data. One notable point is that we cannot select pure secondary charged pion sample. There is non-negligible contribution coming from protons. Figure 11 shows that both data and MC have proton contributions which overlap with charged pion distributions at low E_K regions.

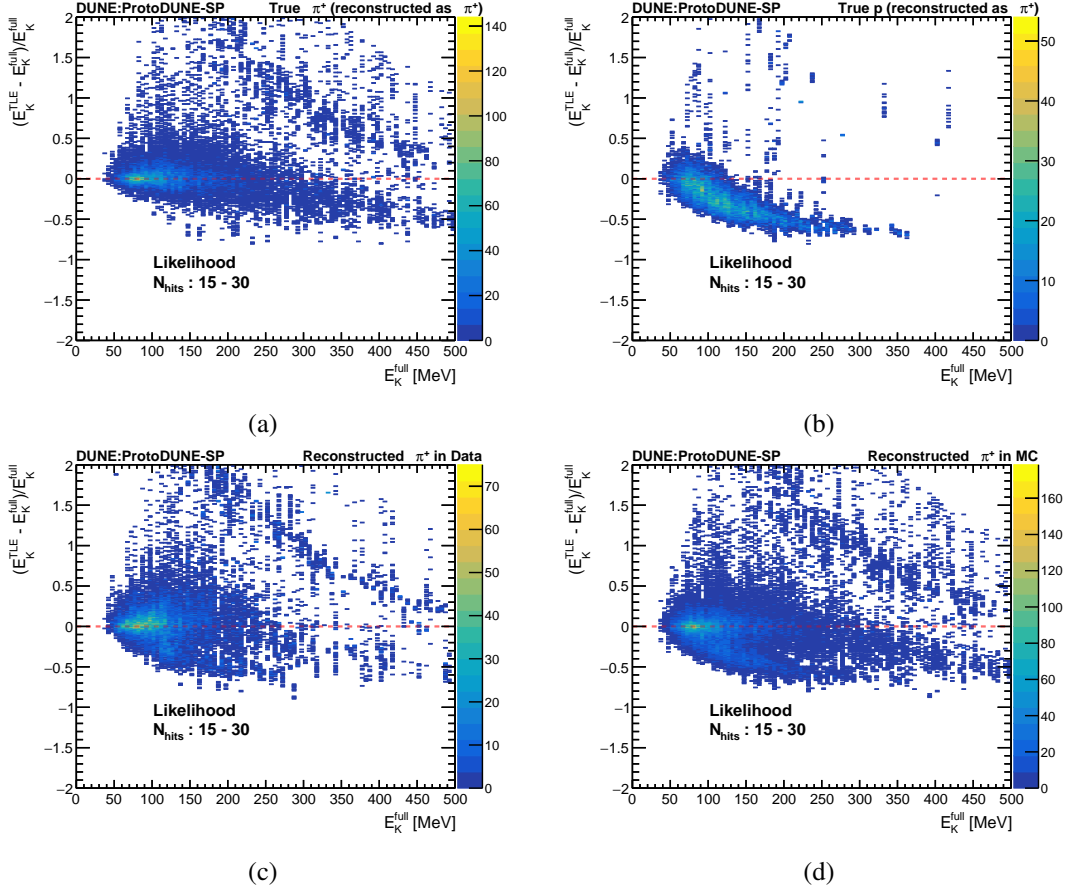


Figure 11: Example two-dimensional distributions of the fractional energy residual using E_K^{full} as reference. Results are coming from reconstructed charged pions with 15 to 30 hits. Top plots show results for MC true pions (left) and true protons (right). Bottom plots show results using all reconstructed charged pions for data (left) and MC sample (right).

The same overlap is observed in one-dimensional distributions of the fractional energy residual as shown in figures 12 and 13. MC simulation and data samples show different proton contributions. It implies that a selection efficiency correction should be made, which is beyond the scope of this study. To deal with the overlap between charged pions and protons, fractional bias distributions are fit using a double Gaussian function. Initial values of the two Gaussian function parameters are set using single Gaussian fit parameters coming from pure charged pion and pure proton distributions of the MC simulation sample. The energy measurement resolution and the fractional bias are

calculated using data points within two standard deviations of the charged pion part Gaussian after subtracting the proton part Gaussian function's contribution. For the case where mean values of two Gaussian functions have difference smaller than 0.1, the proton contribution is not subtracted since the charged pion and the proton contributions are not distinguishable.

Figure 14 summarizes the energy measurement performance for a pure sample of secondary charged pions from the MC simulation. Figure 15 shows a direct performance comparison between data and MC simulation samples. The upper E_K cutoff for each number of hits range is lower than that in figure 14 to ensure good modeling of the proton contribution. The top plot of figure 15 shows good agreement between MC and data in resolution with values smaller than 8%. The bottom plot of figure 15 shows a fractional bias result that is smaller than 10% with discrepancy between MC simulation and data. It means that there should be studies of the energy scale correction and the corresponding systematic uncertainty in order to utilize the TLEFit method. The energy scale correction can be measured at any LArTPC using stopping secondary charged pions from neutrino interactions as introduced in this section, but as a function of E_K^{TLE} rather than the E_K^{full} . Section 6.5 describes the corresponding systematic uncertainty estimates, separately for each source.

An additional comment is that the TLEFit method does not work well for a track for which the dE/dx values have yet to sample the Bragg peak. It is a major reason why there is an upper E_K cutoff for each number of hits range. It is an energy measurement method mainly for charged pions with E_K less than 400 MeV. In this energy region, the most dominant inelastic scattering topology between charged pions and argon nuclei is absorption.

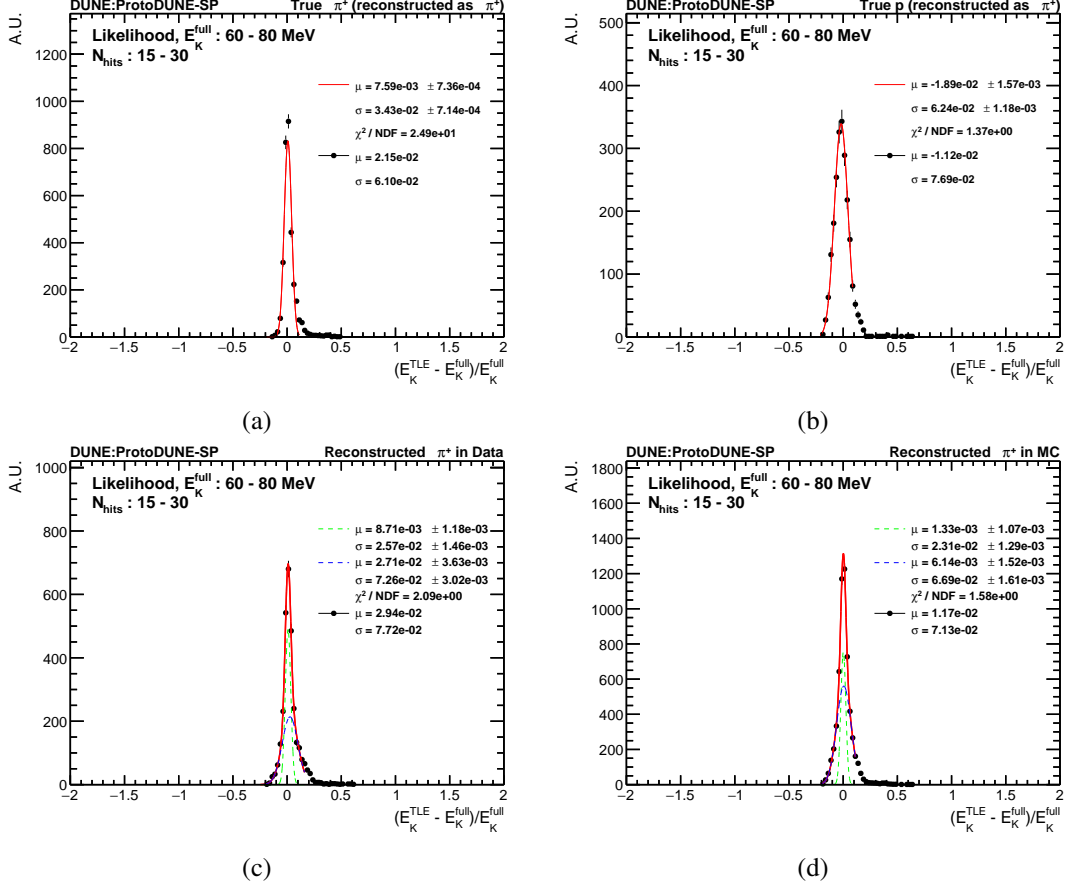


Figure 12: Example distributions of the fractional energy residual using range-based E_K as reference. Results are coming from reconstructed charged pions with 15 to 30 hits and E_K^{full} from 60 MeV to 80 MeV. Top plots show results for MC true pions (a) and true protons (b). Bottom plots show results using all reconstructed charged pions for data (c) and MC sample (d), where green and blue Gaussian functions represent charged pion and proton contributions, respectively.

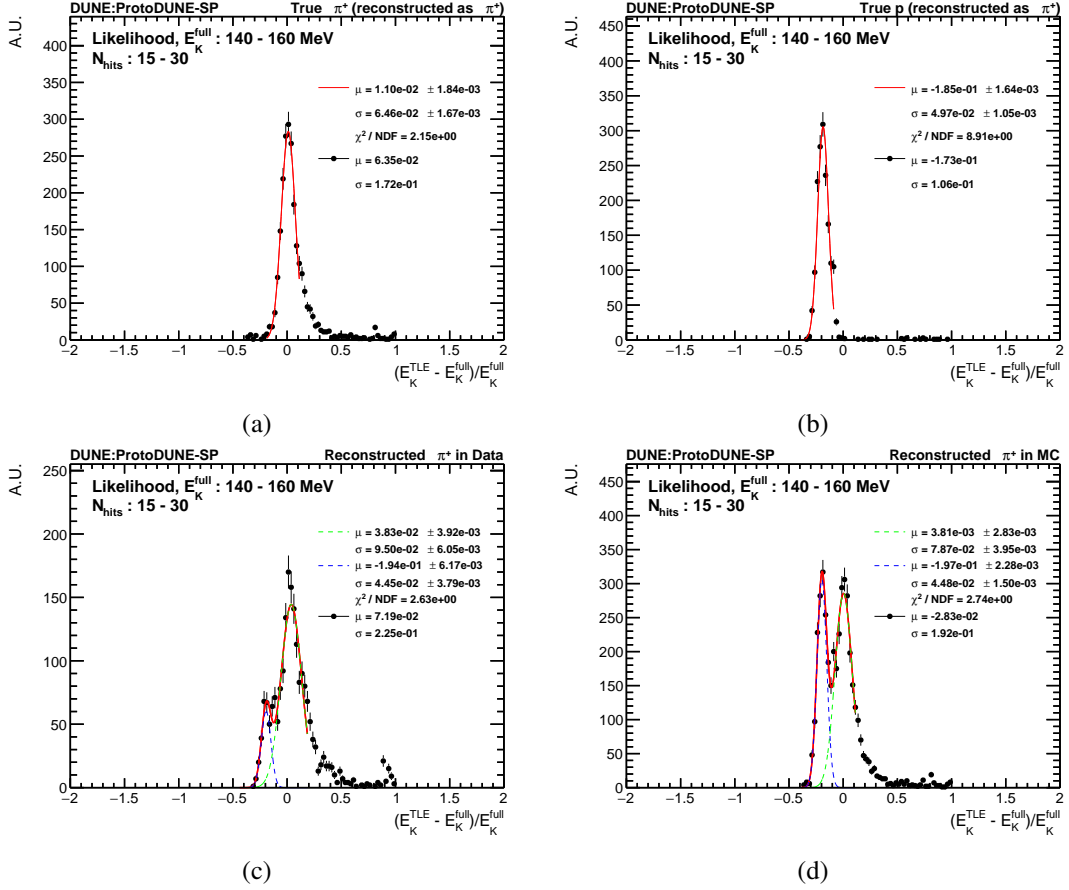


Figure 13: Example distributions of the fractional energy residual using range-based E_K as reference. Results come from reconstructed charged pions with 15 to 30 hits and E_K^{full} from 140 MeV to 160 MeV. Top plots show results for MC true pions (a) and true protons (b). Bottom plots show results using all reconstructed charged pions for data (c) and the MC sample (d), where green and blue Gaussian functions represent charged pion and proton contributions, respectively.

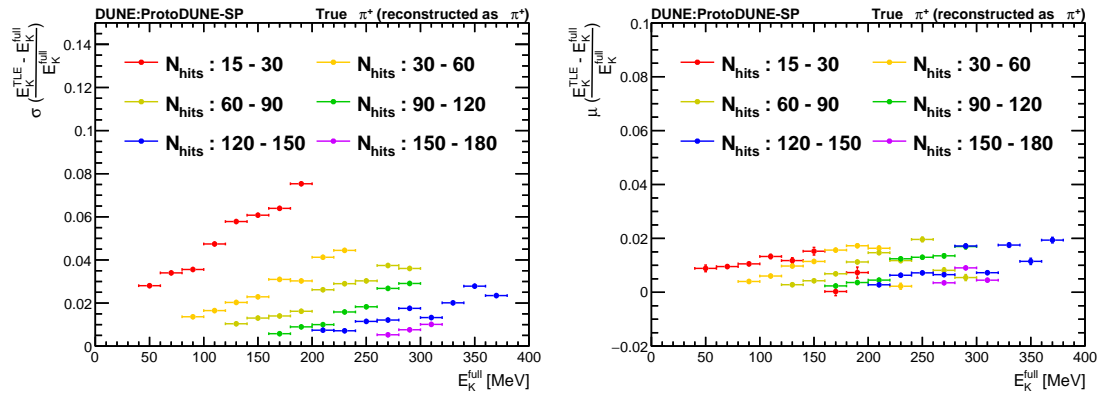


Figure 14: Summarized plots of energy measurement performance of the TLEFit method based on the maximum-likelihood method. Resolutions (left) and fractional biases (right) are shown as functions of charged pions' range-based E_K and number of hits. Pure secondary charged pions are selected from the MC sample.

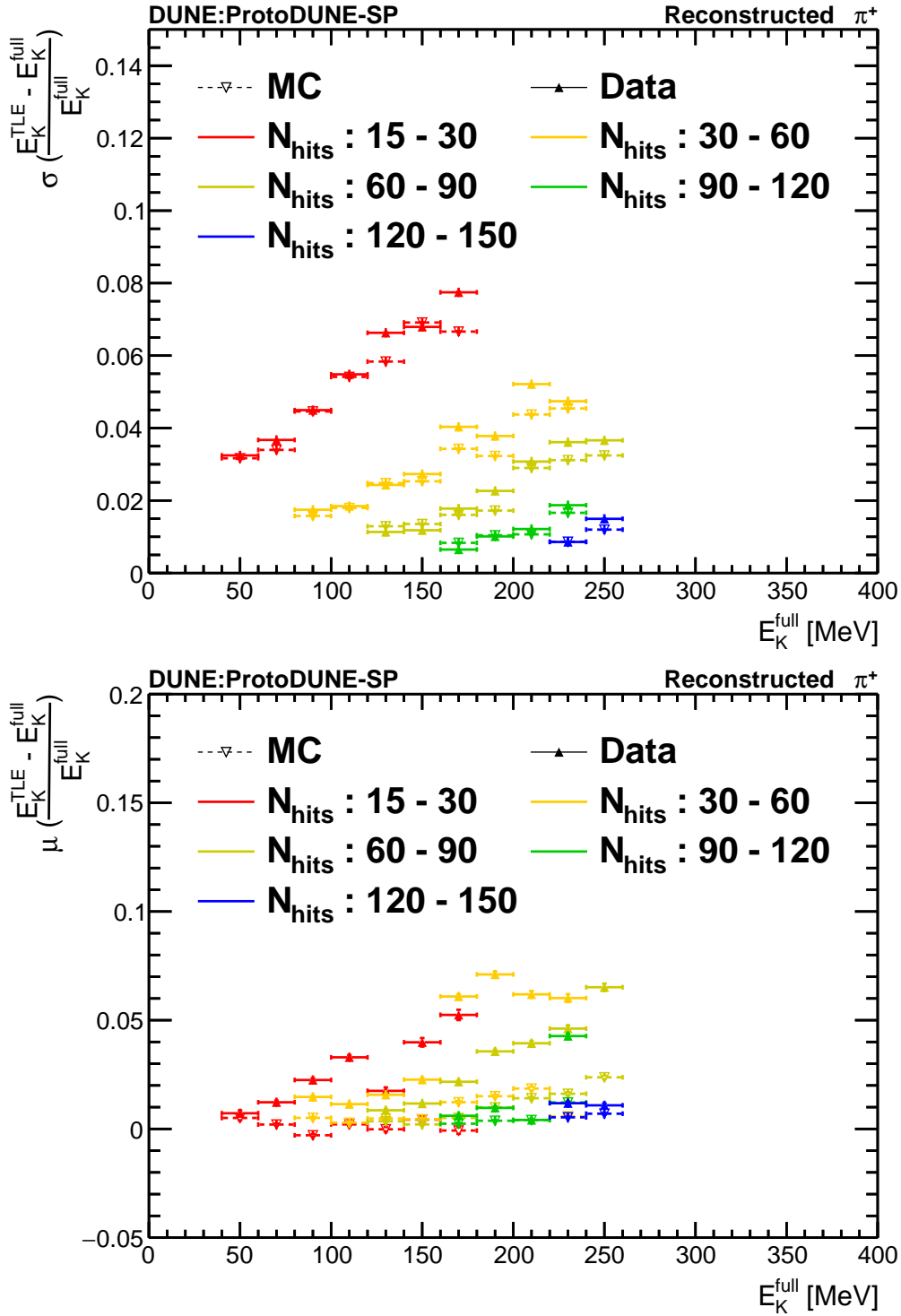


Figure 15: Summarized plots of energy measurement performance of the TLEFit method based on maximum-likelihood method. Resolutions (left) and fractional biases (right) are shown as functions of charged pions' range-based E_K and number of hits. All reconstructed secondary charged pions passing the stopping charged pion cut are used. Monte Carlo points are shown with dashed horizontal bars and the data points are shown with solid horizontal bars.

6.5 Impact of dE/dx modeling

Small discrepancies are seen between data and MC simulation, and these motivate ionization scale and resolution corrections with corresponding systematic uncertainties. Estimations of these corrections are needed in order to use the TLEFit method for physics analyses. In this section, we present the impact of dE/dx modeling on results in figure 15 to understand the discrepancy between MC and data in the fractional bias. Motivation of testing dE/dx modeling is that data shows up to about 7% fractional bias with respect to the range-based energy using full track length while MC sample has less than 2.5% fractional bias. We observe that dE/dx modeling could explain the discrepancy.

Reconstruction of dE/dx for a hit is performed with the following steps. First, ADC values are integrated over time ticks to measure total collected electric charge for the hit. Subsequently, a correction is applied to remove the effect of electron attachment during the drift. Then, a calibration factor (C_{cal}) is multiplied to convert the total electric charge into number of electrons. Finally, total number of electrons is converted into deposited energy based on an assumption that the particle deposits energy only through ionizing argon atoms. The methods for determining C_{cal} and the electron attachment rate from the experimental data are described in Ref. [9].

Recombination between argon ions and electrons has a significant impact on conversion between collected electric charge per unit length dQ/dx [electrons/cm] and dE/dx [MeV/cm]. Thus, it should be modeled. The ProtoDUNE-SP experiment uses the modified box model [28] to consider electron recombination. In this model, the relation between dQ/dx and dE/dx is

$$\frac{dQ}{dx} = \frac{1}{\rho\epsilon\beta'W_{\text{Ion}}} \log \left(\rho\epsilon\beta' \frac{dE}{dx} + \alpha \right), \quad (6.2)$$

where ϵ is the electric field strength, W_{Ion} is mean ionization energy of an argon atom in MeV, and α and β' are the model parameters. For both data production and simulation, the modified box model parameters presented in [28], $\alpha = 0.93 \pm 0.02$ and $\beta' = 0.212 \pm 0.002$ (kV/cm)(g/cm²)/MeV, are used.

The calibration constant is measured using stopping cosmic muons and their minimum ionizing hits. The minimum ionizing hits are selected using kinetic energies measured by the CSDA in the range from 250 MeV to 450 MeV. For a fixed C_{cal} value, dE/dx distributions are drawn as a function of muon E_K bin. Each dE/dx distribution is fitted using a convolution of a Landau function and a Gaussian to measure the most probable value (MPV). Then, a χ_{cal}^2 variable is defined as

$$\chi_{\text{cal}}^2 = \sum_i (\text{MPV}_{\text{fitted},i} - \text{MPV}_{\text{Vavilov},i})^2 / \sigma_{\text{MPV}_{\text{fitted},i}}^2, \quad (6.3)$$

where the index i runs for different E_K bins, $\text{MPV}_{\text{Vavilov},i}$ is expected MPV given by the theory [29], and $\sigma_{\text{MPV}_{\text{fitted},i}}$ is the error of the fitted MPV. The C_{cal} value that gives the minimum χ_{cal}^2 is selected as the calibration constant. In this way, we can achieve a good agreement between data and MC simulation for the MPV of the dE/dx distribution of MIPs.

As a result, figure 16-(d) shows good agreement between data and MC simulation for dE/dx distributions of beam muon hits in a residual range region from 95 to 96 cm, which corresponds to the MIP region. But, for hits near the Bragg peak region, the agreement between data and MC simulation deteriorates as shown in the plots with shorter residual ranges of figure 16. It means

that the modified box model with parameters in [28] cannot describe the recombination effect in ProtoDUNE-SP in the MIP region and the Bragg peak region at the same time. It is well illustrated in figure 17a. The abscissa shows fitted MPVs of MC simulation sample for beam muon hits in residual range region from 2 to 100 cm with 1 cm step. The ordinate shows the ratio of fitted MPV between MC simulation and data in each residual range region. MPV ratio is close to unity where MC simulation MPV is smaller than 1.7 MeV/cm. With increasing MC simulation MPV values, the ratio goes down to about 0.985 and goes up to about 1.04. To understand the impact of such differences in the dE/dx probability density function between data and MC simulation on fractional bias results shown in figure 15, we performed studies described below.

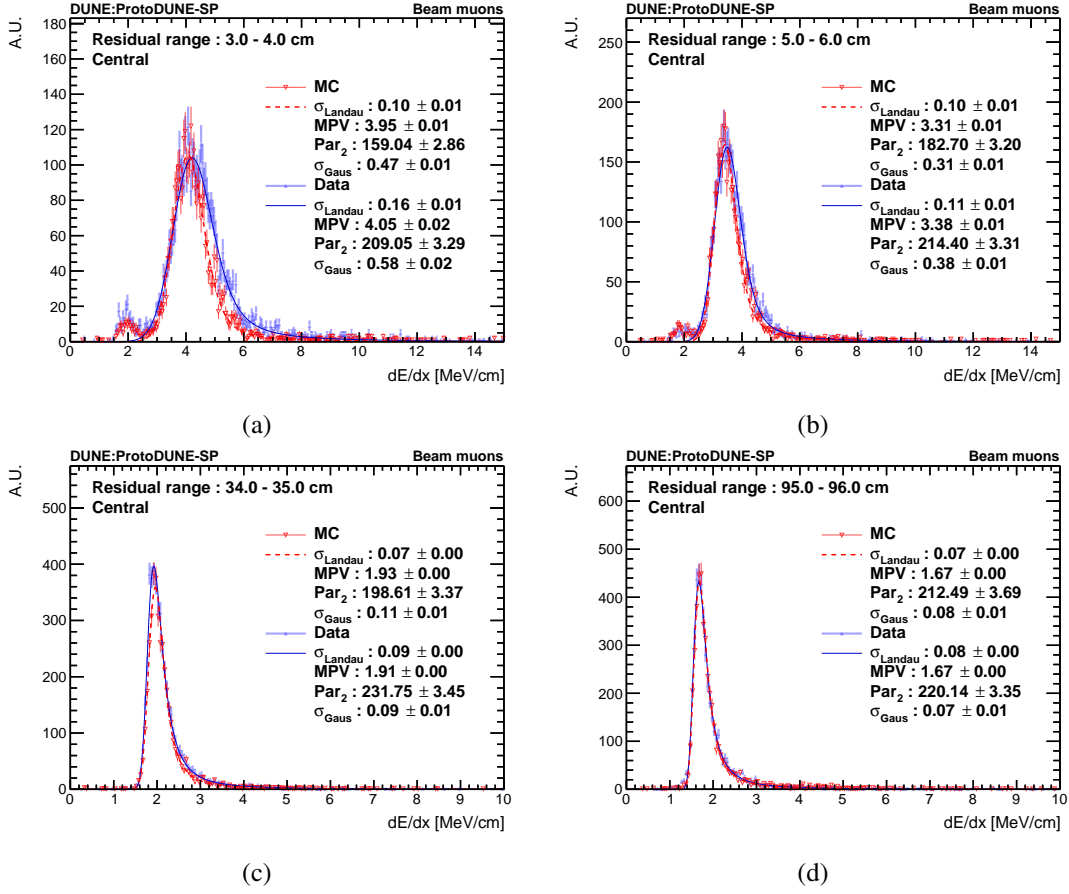


Figure 16: The dE/dx of beam muons is shown as a function of residual range for both data (blue) and MC (red). The results of fits to a Landau function convoluted with a Gaussian are also shown in the legends. The σ_{Landau} is intrinsic width of the Landau function, MPV is fitted most probable value, Par_2 is normalization factor, and σ_{Gaus} is the width of the Gaussian.

6.5.1 Reproduction of data dE/dx distributions

We attempt to reproduce the data's dE/dx distributions by applying scale corrections to the MC simulation sample's dE/dx values. The distribution of the MPV ratio between MC simulation and

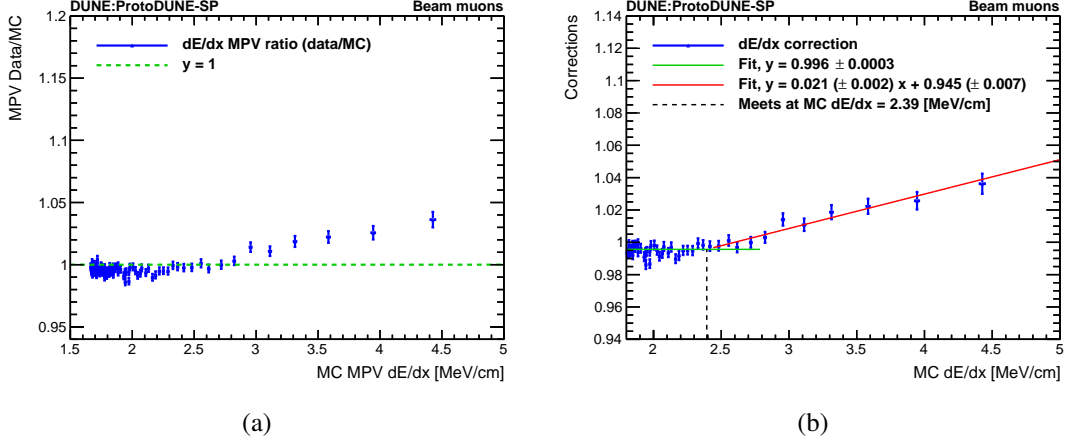


Figure 17: Ratio of fitted MPV values between MC and data as a function of MC MPV. Each MPV value is fitted using beam muon’s hits with a 1 cm interval in residual range from 2 to 100 cm. Ratio is calculated for each residual range interval. Vertical error bars show statistical uncertainties only. Figure (a) shows the ratio distribution with respect to the unity. Figure (b) shows how the dE/dx correction for the Bragg peak region is derived using a linear fit.

data, as shown in figure 17b, is fitted using two linear functions: one flat function for the MIP region and the other with a slope for the Bragg peak region, to derive the scale corrections. It is shown that the two linear functions intersect at a dE/dx value of 2.39 MeV/cm. Consequently, the scale correction for the Bragg peak region is applied to hits with dE/dx greater than 2.39 MeV/cm. As a result, figure 18 shows improved agreement in MPV values between data and MC simulation in the Bragg peak region compared to the state before applying the correction, as shown in figure 16. Note that widths of the Gaussian contribution also have better agreements in the Bragg peak region after applying the scale correction, but with non-negligible differences with respect to their statistical uncertainties. For the MIP region, we test two constant scale corrections with 0.985 and 0.975 to consider the discrepancy for dE/dx from 1.8 MeV/cm to 2.3 MeV/cm shown in figure 17b.

6.5.2 Modified box model parameter uncertainties

Another important point to note here is that shifting the modified box model parameters by one standard deviation can change dE/dx distributions significantly in the Bragg peak region as shown in figure 19. Therefore, a corresponding systematic uncertainty should be considered for the TLEFit algorithm’s performance results in figure 15 for data. The study shown in Section 6.4 is repeated for data with the modified box model parameters shifted up and down by one standard deviations which gives 8 sets of α and β' besides the central set as shown in Table 2. The envelope among the 8 systematic variations is taken as systematic uncertainty for each fractional bias and resolution data point.

6.5.3 Impact on $\chi^2_{\pi^\pm}$

Differences in the dE/dx probability density functions between data and MC also affect the stopping charged pion selection. It is required that reconstructed secondary charged pions should have

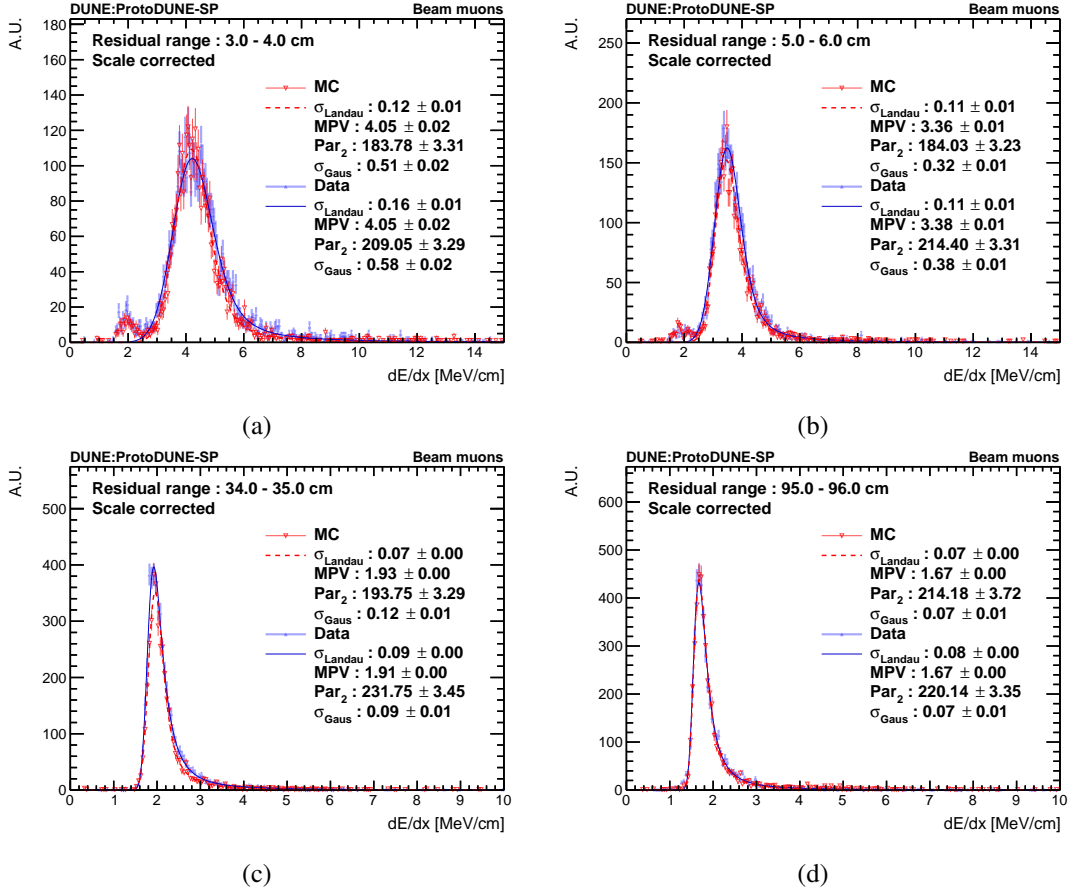


Figure 18: The measured dE/dx values for hits along beam muon tracks are shown as a function of residual range for both data (blue) and MC (red). Fitting results with the convoluted functions of the Gaussian and the Landau functions are also shown in the legends. The parameter σ_{Landau} is the intrinsic width of the Landau function, MPV is the fitted most probable value, Par_2 is the normalization factor, and σ_{Gaus} is the width of the Gaussian part. The scale correction shown in figure 17b for dE/dx values is applied for MC sample.

Table 2: Recombination parameter shifts that are used for the study based on ArgoNeUT's measurement [28].

	α	$\beta' [(kV/cm)(g/cm^2)/MeV]$
Central	0.93	0.212
Systematic variations	0.93	0.210
	0.91	0.214
	0.91	0.210
	0.91	0.212
	0.91	0.214
	0.95	0.210
	0.95	0.212
	0.95	0.214

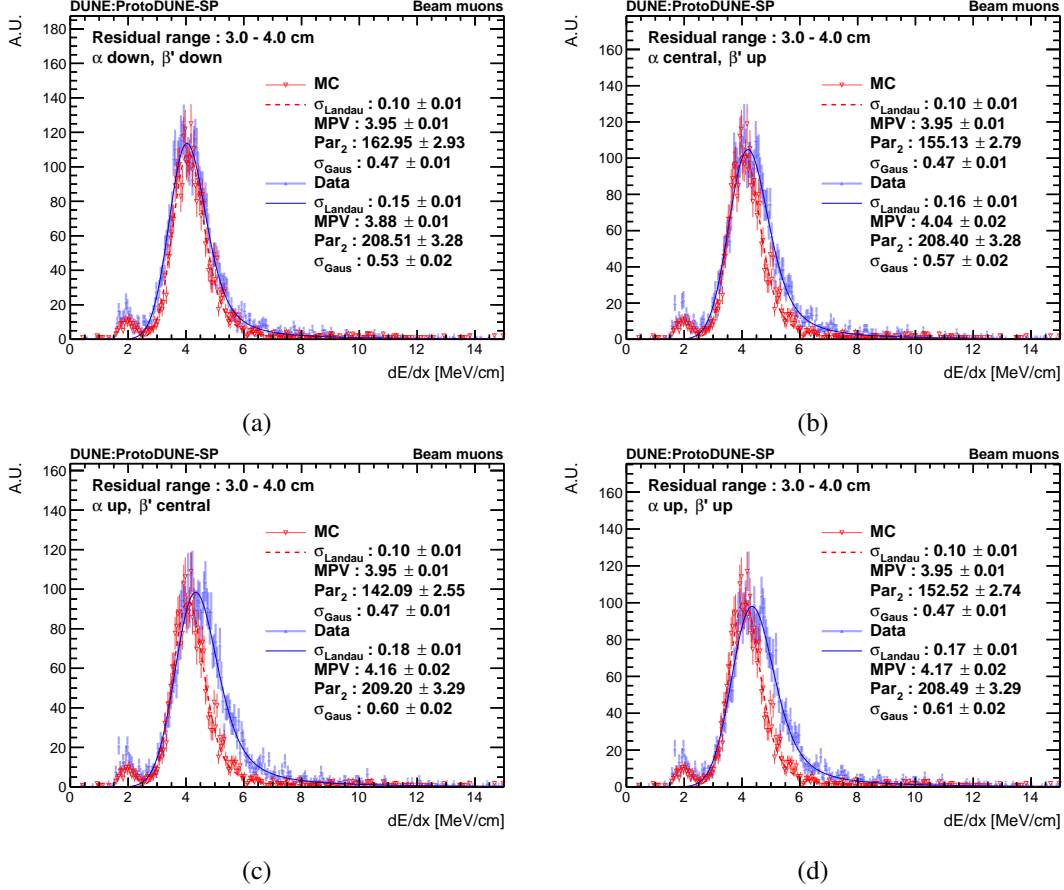


Figure 19: The measured dE/dx values of hits along beam muon tracks are shown for residual ranges between 3 and 4 cm for data (blue) and MC (red). Fitting results with the convoluted functions of the Gaussian and the Landau functions are also shown in the legends. The parameter σ_{Landau} is the intrinsic width of the Landau function, MPV is the fitted most probable value, Par_2 is the normalization factor, and σ_{Gaus} is the width of the Gaussian component. Modified box model parameters are each shifted by one standard deviation [28] for data. Distributions of MC are the same in each of the four plots.

$\chi^2_{\pi^\pm}$ smaller than 6. The amount of contribution coming from interacting charged pions is different between data and MC simulation with the same $\chi^2_{\pi^\pm}$ cut because measured dE/dx values are included in Eq. 6.1 and there are discrepancies between the data and MC simulation dE/dx measurements. Therefore, the $\chi^2_{\pi^\pm}$ with dE/dx values after corrections are used to select stopping charged pions in two studies above.

6.5.4 Results

Figures 20 and 21 summarize the track length-fitting method's performance results derived from the studies described above. Energy measurement resolution results are stable. For fractional biases, there are two points to note here. The first point is about dE/dx scale corrections for the MC

sample. While the correction factor for dE/dx values exceeding 2.39 MeV/cm can reach up to 5%, and the correction for dE/dx values in the range of 1.8 to 2.3 MeV/cm can reach up to 2.5%, the latter correction has a more significant impact on the fractional bias result. This can be understood from the slope of the Bethe-Bloch formula as a function of residual range shown in figure 1. A few-percent shift in dE/dx could lead to a larger change in the residual range for small dE/dx values compared to large dE/dx values since the slope of the energy loss function is falling down as a function of residual range. It can also explain the tendency shown in central data that charged pions with higher E_K show larger fractional biases in their measured E_K . The second point is that shifts in modified box model parameters for data have significant impact on fractional bias results. These two points conclude that better understanding of dE/dx measurements leads to smaller systematic uncertainty on the scale of measured E_K by the TLEFit method.

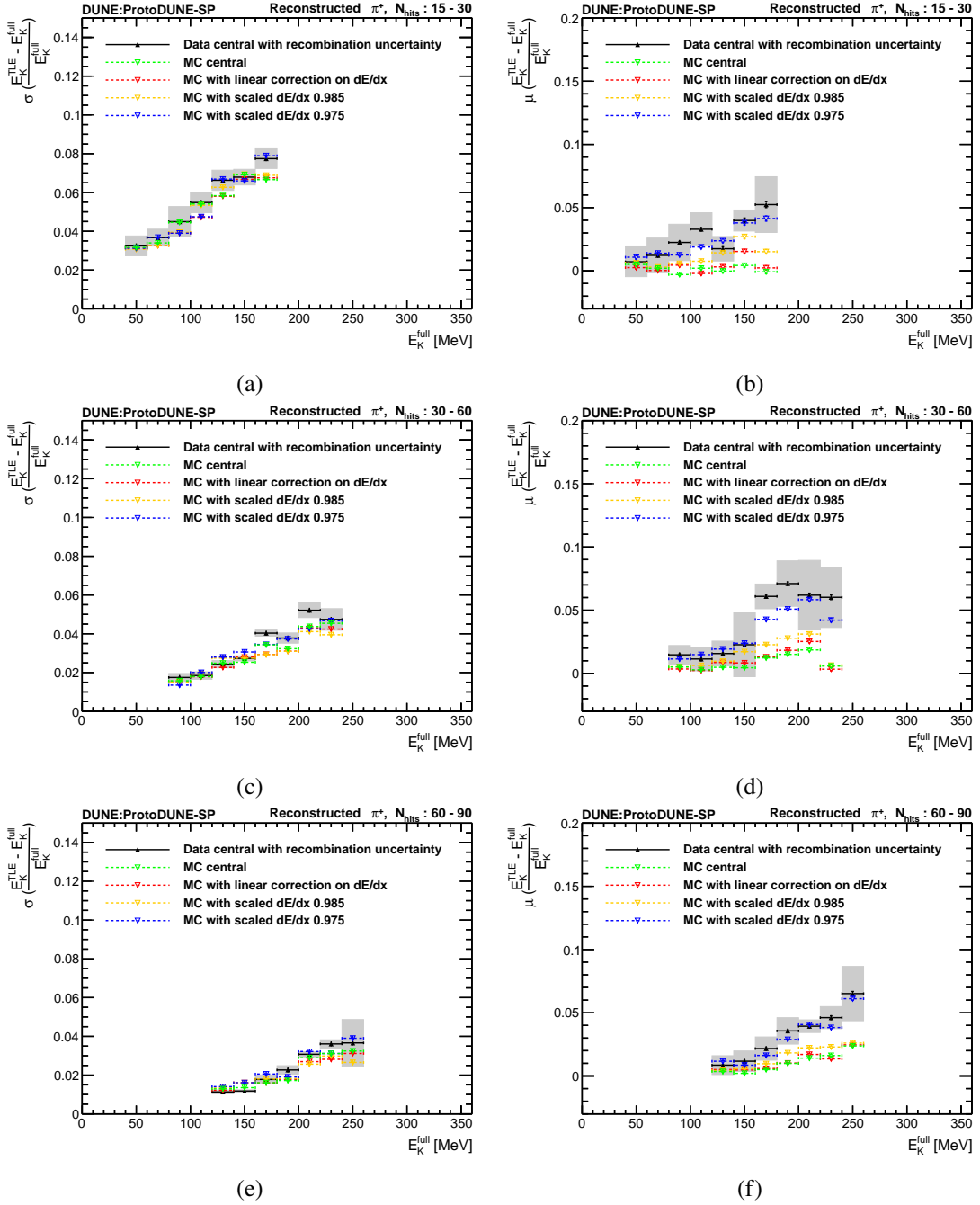


Figure 20: Summary of studies considering the impact of dE/dx modeling. Resolutions (left) and fractional biases (right) are shown as functions of charged pions' E_K^{full} and the number of hits (top: 15 to 30 hits, middle: 30 to 60 hits, and bottom: 60 to 90 hits). Black points show data results with gray error bars that are measured with biggest differences between data and 8 sets of shifted modified box model parameters. Green points show central MC results. Red points show results with linear scale correction on MC that is shown as a red solid line in figure 17b. Orange and blue points show results with constant dE/dx scale corrections on MC with 0.985 and 0.975, respectively.

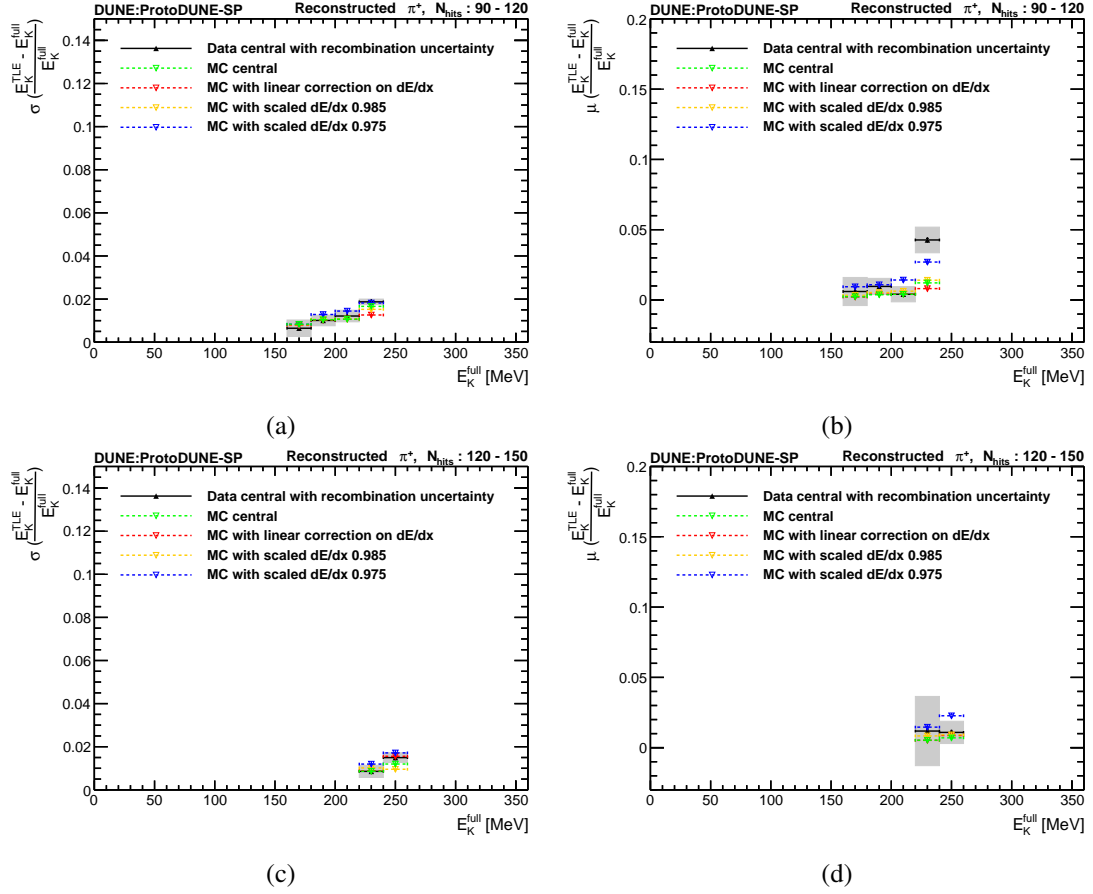


Figure 21: Summary of studies considering the impact of dE/dx modeling. Resolutions (left) and fractional biases (right) are shown as functions of charged pions' E_K^{full} and the number of hits (top: 90 to 120 hits and bottom: 120 to 150 hits). Black points show data results with gray error bars that are measured with biggest differences between data and 8 sets of shifted modified box model parameters. Green points show central MC results. Red points show results with linear scale correction on MC that is shown as a red solid line in figure 17b. Orange and blue points show results with constant dE/dx scale corrections on MC with 0.985 and 0.975, respectively.

7 Summary

We introduce the track-length extension fitting (TLEFit) algorithm for measuring the kinetic energies of inelastically interacting particles in liquid argon time projection chambers. The algorithm's performance for charged pion energy measurement is studied in detail using secondary charged pions from data collected by the ProtoDUNE-SP detector with a 1 GeV/ c charged pion beam and in a corresponding Monte Carlo sample. For charged pion tracks with kinetic energy (E_K) less than 400 MeV and with the Bragg peak signature, the energy resolution is better than 6.5%, and the fractional bias is less than 4% for MC sample using true E_K as reference. For direct comparison of the performance between the data and the MC samples, range-based E_K is used as a reference after a validation that it can describe the true E_K well for charged pions passing a selection based on $\chi^2_{\pi^\pm}$. After subtracting the proton contribution from distributions of the fractional energy residual, the resolution is measured to be better than 8% (7%), and the fractional bias is smaller than 8% (3%) for the data (MC simulation) sample. Differences between the data and MC simulation samples are considered in order to calculate the energy scale correction and the systematic uncertainty on the scale and resolution. Additional studies find that the resolution results are stable and the fractional bias results are sensitive to the dE/dx scale in the MIP region and also to the recombination model. Since the algorithm fits for the expected total track length until the particle would stop for an incomplete track, it can be used to measure the energies of charged pions absorbed by argon nuclei in the detector material. Absorption is the dominant inelastic scattering interaction between charged pions and argon nuclei for charged-pion kinetic energies less than 300 MeV. In addition, the method of using stopping secondary charged pions to characterize the energy measurement performance can be used in any LArTPC by collecting neutrino interaction events with stopping charged pions in the final state.

Acknowledgments

The ProtoDUNE-SP detector was constructed and operated on the CERN Neutrino Platform. We gratefully acknowledge the support of the CERN management, and the CERN EP, BE, TE, EN and IT Departments for NP04/ProtoDUNE-SP.

This document was prepared by the DUNE collaboration using the resources of the Fermi National Accelerator Laboratory (Fermilab), a U.S. Department of Energy, Office of Science, HEP User Facility. Fermilab is managed by Fermi Research Alliance, LLC (FRA), acting under Contract No. DE-AC02-07CH11359.

This work was supported by CNPq, FAPERJ, FAPEG and FAPESP, Brazil; CFI, IPP and NSERC, Canada; CERN; MŠMT, Czech Republic; ERDF, Horizon Europe, MSCA and NextGenerationEU, European Union; CNRS/IN2P3 and CEA, France; INFN, Italy; FCT, Portugal; NRF, South Korea; Generalitat Valenciana, Junta de Andalucía-FEDER, MICINN, and Xunta de Galicia, Spain; SERI and SNSF, Switzerland; TÜBİTAK, Turkey; The Royal Society and UKRI/STFC, United Kingdom; DOE and NSF, United States of America.

References

- [1] SUPER-KAMIOKANDE collaboration, *Evidence for oscillation of atmospheric neutrinos*, *Phys. Rev. Lett.* **81** (1998) 1562.
- [2] SNO collaboration, *Direct evidence for neutrino flavor transformation from neutral-current interactions in the Sudbury Neutrino Observatory*, *Phys. Rev. Lett.* **89** (2002) 011301.
- [3] M. Fukugita and T. Yanagida, *Baryogenesis Without Grand Unification*, *Phys. Lett. B* **174** (1986) 45.
- [4] C. Rubbia, *The Liquid Argon Time Projection Chamber: A New Concept for Neutrino Detectors*, .
- [5] DUNE collaboration, *Snowmass Neutrino Frontier: DUNE Physics Summary*, [2203.06100](#).
- [6] A. Friedland and S.W. Li, *Understanding the energy resolution of liquid argon neutrino detectors*, *Phys. Rev. D* **99** (2019) 036009 [[1811.06159](#)].
- [7] J.A. Formaggio and G.P. Zeller, *From eV to EeV: Neutrino Cross Sections Across Energy Scales*, *Rev. Mod. Phys.* **84** (2012) 1307 [[1305.7513](#)].
- [8] DUNE collaboration, *Design, construction and operation of the ProtoDUNE-SP liquid argon TPC*, *JINST* **17** (2022) P01005 [[2108.01902](#)].
- [9] DUNE collaboration, *First results on ProtoDUNE-SP liquid argon time projection chamber performance from a beam test at the CERN neutrino platform*, *JINST* **15** (2020) P12004 [[2007.06722](#)].
- [10] PARTICLE DATA GROUP collaboration, *Review of Particle Physics*, *Prog. Theor. Exp. Phys.* **2022** (2022) 083C01.
- [11] MICROBOONE collaboration, *Determination of muon momentum in the MicroBooNE LArTPC using an improved model of multiple Coulomb scattering*, *JINST* **12** (2017) P10010 [[1703.06187](#)].
- [12] LArIAT collaboration, *The Liquid Argon In A Testbeam (LArIAT) Experiment*, *JINST* **15** (2020) P04026 [[1911.10379](#)].
- [13] MICROBOONE collaboration, *First Measurement of Energy-Dependent Inclusive Muon Neutrino Charged-Current Cross Sections on Argon with the MicroBooNE Detector*, *Phys. Rev. Lett.* **128** (2022) 151801 [[2110.14023](#)].
- [14] C. Anderson et al., *The ArgoNeuT Detector in the NuMI Low-Energy Beam Line at Fermilab*, *JINST* **7** (2012) P10019 [[1205.6747](#)].
- [15] P.V. Vavilov, *Ionization losses of high-energy heavy particles*, *Sov. Phys. JETP* **5** (1957) 749.
- [16] R. Brun, F. Bruyant, F. Carminati, S. Giani, M. Maire, A. McPherson et al., *GEANT Detector Description and Simulation Tool*, .
- [17] H. Bichsel, *Straggling in Thin Silicon Detectors*, *Rev. Mod. Phys.* **60** (1988) 663.
- [18] DUNE collaboration, *The single-phase protodune technical design report*, [1706.07081](#).
- [19] DUNE collaboration, *Deep Underground Neutrino Experiment (DUNE), Far Detector Technical Design Report, Volume IV: Far Detector Single-phase Technology*, *JINST* **15** (2020) T08010 [[2002.03010](#)].
- [20] N. Charitonidis and I. Efthymiopoulos, *Low energy tertiary beam line design for the cern neutrino platform project*, *Phys. Rev. Accel. Beams* **20** (2017) 111001.

- [21] A.C. Booth, N. Charitonidis, P. Chatzidaki, Y. Karyotakis, E. Nowak, I. Ortega-Ruiz et al., *Particle production, transport, and identification in the regime of 1 – 7 GeV/c*, *Phys. Rev. Accel. Beams* **22** (2019) 061003.
- [22] S. Agostinelli et al., *Geant4—a simulation toolkit*, *Nuclear Instruments and Methods in Physics Research Section A: Accelerators, Spectrometers, Detectors and Associated Equipment* **506** (2003) 250.
- [23] Muons, Inc., “G4beamline.” <http://g4beamline.muonsinc.com>.
- [24] D. Heck, J. Knapp, J.N. Capdevielle, G. Schatz and T. Thouw, *CORSIKA: A Monte Carlo code to simulate extensive air showers*, .
- [25] E.D. Church, *LArSoft: A Software Package for Liquid Argon Time Projection Drift Chambers*, [1311.6774](#).
- [26] MICROBoONE collaboration, *Wire-cell 3D pattern recognition techniques for neutrino event reconstruction in large LArTPCs: algorithm description and quantitative evaluation with MicroBoONE simulation*, *JINST* **17** (2022) P01037 [[2110.13961](#)].
- [27] DUNE collaboration, *Reconstruction of interactions in the ProtoDUNE-SP detector with Pandora*, *Eur. Phys. J. C* **83** (2023) 618 [[2206.14521](#)].
- [28] ARGONeUT collaboration, *A Study of Electron Recombination Using Highly Ionizing Particles in the ArgoNeUT Liquid Argon TPC*, *JINST* **8** (2013) P08005 [[1306.1712](#)].
- [29] H. Bichsel, *Straggling in thin silicon detectors*, *Rev. Mod. Phys.* **60** (1988) 663.